Masterarbeit

Evanescent Two Photon Spectroscopy of Rubidium Atoms for Integrated Silicon Structures at Telecom Wavelength

vorgelegt von

Artur Skljarow

am 5. Juli 2018

Hauptberichter: Prof. Dr. Tilman Pfau

Mitberichter: Prof. Dr. Jörg Wrachtrup

5. Physikalisches Institut
Universität Stuttgart

Ehrenwörtliche Erklärung

Ich erkläre,

- dass ich diese Masterarbeit selbständig verfasst habe,
- dass ich keine anderen als die angegebenen Quellen benutzt und alle wörtlich oder sinngemäß aus anderen Werken übernommenen Aussagen als solche gekennzeichnet habe,
- dass die eingereichte Arbeit weder vollständig noch in wesentlichen Teilen Gegenstand eines anderen Prüfungsverfahrens gewesen ist,
- dass ich die Arbeit weder vollständig noch in Teilen bereits veröffentlicht habe, es sei denn, der Prüfungsausschuss hat die Veröffentlichung vorher genehmigt
- und dass der Inhalt des elektronischen Exemplars mit dem des Druckexemplars übereinstimmt.

Stuttgart, den 5. Juli 2018

Artur Skljarow

Abstract

In the presented work the behavior of thermal rubidium atoms interacting with light in the vicinity of a silicon surface is studied. The total internal reflection of a laser beam from a silicon surface allows the evanescent field to penetrate into the atomic vapor. The reflected signal carries information about the atom light interaction. An additional laser is added in order to study the two-photon transition to the 4D states regarding the intensity, density, temperature, and penetration depth.

In the frame work of this thesis a suitable experimental spectroscopy setup has been built and novel measurements of evanescent 4D spectra of rubidium have been demonstrated. The results of this work pave the path to investigate integrated silicon structures in thermal atomic vapor.

In der vorliegenden Arbeit wird das Verhalten von heißen Rubidiumatomen, die in der Nähe einer Siliziumoberfläche mit Licht wechselwirken, untersucht. Durch Totalreflexion an dieser Oberfläche entsteht ein evaneszentes Feld, welches in das atomare Gas eindringt. Der reflektierte Strahl beinhaltet damit Informationen über seine Wechselwirkung mit den Atomen. Ein weiterer Laser wird dazu genutzt, über Zwei-Photonen-Spektroskopie die 4D-Zustände hinsichtlich Intensität, Dichte, Temperatur und Eindringtiefe zu untersuchen.
Im Rahmen dieser Arbeit wurde ein geeignetes Experiment realisiert, welches neuartige Messungen von evaneszenten 4D-Spektren von Rubidium ermöglicht. Die Ergebnisse dieser Arbeit bahnen den Weg für die Untersuchung von integrierten Siliziumstrukturen mit heißen Atomen.

Contents

1. Motivation

Vapor cells filled with alkali atoms have found many applications in fundamental scientific research and our everyday life [1]. Precision measurements and references rely on atomic transitions. The universal definition of a second and the directly related atomic clock use hyperfine levels of rubidium [2] or caesium [3]. This high precision reference finds its applications in satellites for GPS and navigation [4].
Combined with the stability of atomic transitions, vapor cells open a diverse field of high sensitivity sensors for electric field [5], microwave [6] and magnetic field [7] characterization. More sophisticated applications can be found in gas sensors e.g. in nitric oxide [8]. Recently, thermal single photon sources were implemented in vapor cells [9].
The potential in scalability allows the marriage of vapor cells with integrated photonic structures such as waveguides, interferometers, and resonators. This opens a completely new field of data processing and light matter interaction. Studies on integrated silicon nitride structures in a rubidium vapor [10–12] have been carried out in our group at the university of Stuttgart recently. These works have motivated this thesis as a direct follow-up study.
The previously studied waveguides exhibit moderate ohmic losses, hence, an absorption of 780 nm light traveling through the structures. Pure silicon structures show almost no absorption at telecom wavelengths ($\approx$ 1550 nm). The progress in miniaturized silicon chips sets a fabrication benchmark for scalability and quality of the structures. Therefore, the aim is to continue the work on integrated photonic structures in vapor cells with pure silicon.
Due to the larger refractive index of silicon (3.5), the electric field is better confined which leads to a smaller mode volume. The 4D states of rubidium can be accessed via two-photon transition from 5S to 5P at 780 nm and from 5P to 4D at 1529 nm in a ladder scheme. The probe light (1529 nm) will be sent through the silicon structure and the pump light (780 nm) will be shone on the structure from above.
The purpose of this thesis is to build an experimental setup for the excitation of the 4D states and fully characterize them. Afterwards, the compatibility of silicon with rubidium will be tested for temperatures up to 200°C. Finally, the evanescent spectroscopy of rubidium 4D states in the vicinity of the silicon surface will be demonstrated.

Outline

This thesis starts with the derivation of the evanescent fields. The importance of the critical angle is derived and explained. All relevant properties of the evanescent field are presented and visualized.

After discussing the light properties, the interaction of light and matter is presented. There, a two level atom interacting with monochromatic light is studied in detail. The full Hamiltonian of the system is derived and discussed. The optical Bloch equations obtained from this Hamiltonian are solved for the steady state situation and their results are presented. It includes the effects of laser power, decoherence processes, and thermal effects.

The fourth chapter focuses on the experimental setup. The first section describes the settings of the telecom laser at 1529 nm. Values for the beam quality, power, and stability are presented. The next section describes the spectroscopy setup which includes two lasers, one at 1529 nm and the other at 780 nm. The fabrication of the home-built wafer cell is presented in detail which is the core of this experiment. The cell consists of a glass frame closed by a glass and a silicon window with a zinc selenide prism attached to the silicon. This cell allows the evanescent spectroscopy of a thermal vapor with two lasers.

The fifth chapter deals with the hyperfine spectrum of the reference cells. A full analysis together with a fit function is given in order to investigate all effects of the addressed 4D states of rubidium via a two-photon transition from 5S to 5P to 4D in a ladder scheme. The influence of the laser power on both isotopes is studied in co- and counter-propagating configurations of the lasers.

The sixth chapter presents the results of the evanescent spectroscopy. At the beginning, the behavior of the evanescent signal for different atomic densities and temperatures is studied. The broadening of the linewidth is discussed and explained with the aid of the corresponding theory section. The origin of a shift of the wafer spectrum relative to the hyperfine reference is explained. The effects of laser power are studied in comparison to the reference signal from the previous chapter. Moreover, effects of laser polarization on the evanescent signal are studied as well. In the end, the evanescent field is tuned via the angle of incidence into the wafer cell.

The last part of the thesis gives a brief summary of the presented results and mentions some of the follow-up studies based on the results of this thesis.

2. Theory of Evanescent Fields

2.1. Derivation of the Evanescent Field

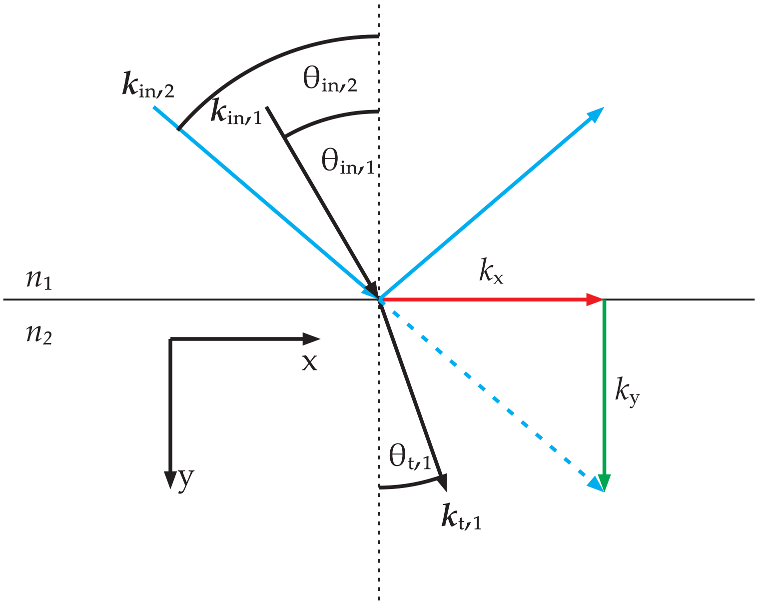

FIGURE 2.1.: Incident planewave below (black) and above (blue) the critical angle at a dielectric boundary between two media with refractive indices n_1 and n_2.

A monochromatic planewave's spatial propagation and time evolution is given by

$$\boldsymbol{E} = \boldsymbol{E}_0 \cdot \exp(i(\boldsymbol{kr} - \omega t)) + c.c., \tag{2.1}$$

where $\boldsymbol{E}_0$ describes the amplitude, $\boldsymbol{r}$ the spatial position, $\omega = 2\pi f$ the angular frequency, and t the time. The direction of propagation is given by $\boldsymbol{k}$ with $|\boldsymbol{k}| = nk_0 = n\omega/c$ and n being the refractive index. In order to understand the effects of evanescent fields one can neglect the time evolution and decompose the spatial propagation into its Cartesian components

$$\boldsymbol{E} = \boldsymbol{E}_0 \cdot \exp(i\boldsymbol{kr}) = \boldsymbol{E}_0 \cdot \exp[ink_0(x\sin(\theta) + y\cos(\theta))]. \tag{2.2}$$

Fig. 2.1 shows the plane of incidence for an planewave at the boundary between two dielectric media with refractive indices n_1 and n_2 with $n_1 > n_2$.
The angle of transmission θ_t for a certain incident angle θ_in can be calculated from Snell's law

$$n_1 \sin(\theta_\mathrm{in}) = n_2 \sin(\theta_\mathrm{t}). \tag{2.3}$$

The black arrows show the case for transmission through the second medium. Blue arrows indicate the case for total reflection at the surface of the medium with a smaller refractive index with a transmission angle of 90°. Note that the reflected part of the incident wave is neglected for the case of angles below the critical angle. Under those condition one can define the critical angle of incidence from Eq. (2.3)

$$\theta_\mathrm{c} = \arcsin\left(\frac{n_2}{n_1}\right). \tag{2.4}$$

This angle highly depends on the change of the refractive index propagating through the boundary. For larger n_2/n_1 the critical angle increases leading to total reflection at smaller angles of incidence.
Propagation of planewaves above the critical angles leads to $\sin(\theta_t) > 1$. In that case one can write

$$\cos(\theta_\mathrm{t}) = i\sqrt{\sin(\theta_\mathrm{t})^2 - 1} = i\sqrt{\left(\frac{\sin(\theta_\mathrm{in})}{\sin(\theta_\mathrm{c})}\right)^2 - 1} \tag{2.5}$$

and

$$\sin(\theta_\mathrm{t}) = \left(\frac{\sin(\theta_\mathrm{in})}{\sin(\theta_\mathrm{c})}\right). \tag{2.6}$$

Then, using the substitution $\alpha = n_1 k_0 \cdot \left(\frac{\sin(\theta_\mathrm{in})}{\sin(\theta_\mathrm{c})}\right)$ and $\beta = n_2 k_0 \cdot \sqrt{\left(\frac{\sin(\theta_\mathrm{in})}{\sin(\theta_\mathrm{c})}\right)^2 - 1}$ the expression for the transmitted electric field reads

$$\boldsymbol{E}_t = \boldsymbol{E}_{0,t} \cdot \exp(i\alpha x - \beta y). \tag{2.7}$$

From Maxwell's boundary conditions one can conclude that α is dependent on the refractive index of the first medium while β contains the refractive index of the second medium.
The wavevector of the electric field now has a real part α propagating along the boundary between the two media, whereas the imaginary component βy exponentially decays into the second medium. This exponential decay represents the so called *evanescent field.* Note that E_t only shows the transmitted part of the incident wave, the reflected wave was neglected for reasons of clarity.

The wavevectors $|k_x| = \alpha$ (red) and $|k_y| = \beta$ (green) are drawn in Fig. 2.1 for total reflection. The next section shows how far the evanescent field penetrates into the second medium and discusses the possibilities to enhance or decrease the evanescent field.

2.2. Penetration Depth

The intensity of the monochromatic planewave is given by

$$I = \frac{1}{2} c n \epsilon_0 |\boldsymbol{E}|^2, \tag{2.8}$$

its propagation through a medium is discribed by Beer-Lambert's law

$$I = I_0 \cdot \exp(-\gamma d), \tag{2.9}$$

with the absorption coefficient γ and the decay length or penetration depth d. For the evanescent decay one usually defines a decrease of the intensity from a maximum of I_0 to $1/\mathrm{e}^2 I_0$. In comparison to the derived electric field from the previous section the penetration depth of the evanescent field is given by

$$d = \frac{2}{\gamma} = \frac{1}{\beta} = \frac{\lambda}{2\pi n_2 \sqrt{\left(\sin(\theta_{\mathrm{in}}) \cdot \frac{n_1}{n_2}\right)^2 - 1}}, \tag{2.10}$$

with $k_0 = \frac{2\pi}{\lambda}$ expressed in terms of the wavelength λ. The penetration depth shows asymptotic divergence for incident angles close to the critical angle where $\sin\theta_{\mathrm{in}}/\sin\theta_{\mathrm{c}}$ becomes 1 in the denominator. Therefore, it is strongly sensitive to changes in the angle of incidence, the refractive indices of both media and slightly dependent on the wavelength.

For the further progress of this experiment the transition from zinc selenide (ZnSe) to glass and from silicon to air is of main importance (compare with Fig. 4.8). The refractive indices of $n_{\mathrm{Si}} = 3.4984$ [13] and $n_{\mathrm{air}} = 1.0003$ [14] lead to a critical angle of $\theta_{\mathrm{Si}\rightarrow\mathrm{air}} = 16.61°$. For the transition from ZnSe into glass the refractive index changes from $n_{\mathrm{ZnSe}} = 2.4488$ [15] to $n_{\mathrm{glass}} \approx 1.5318$ which results in a critical angle of $\theta_{\mathrm{ZnSe}\rightarrow\mathrm{glass}} = 38.72°$. All values for the refractive indices are given at a wavelength of 1529 nm except the value for glass which is measured at 589 nm. The penetration depth for those two cases is plotted in Fig. 2.2 over the angles of incidence and is on a scale of $\lambda/(2\pi)$. It drops significantly going further above the critical angle. For small changes towards angles below θ_{C}, transmission starts to happen on a very fine scale due to the divergence at θ_{C}. Thus, changes around

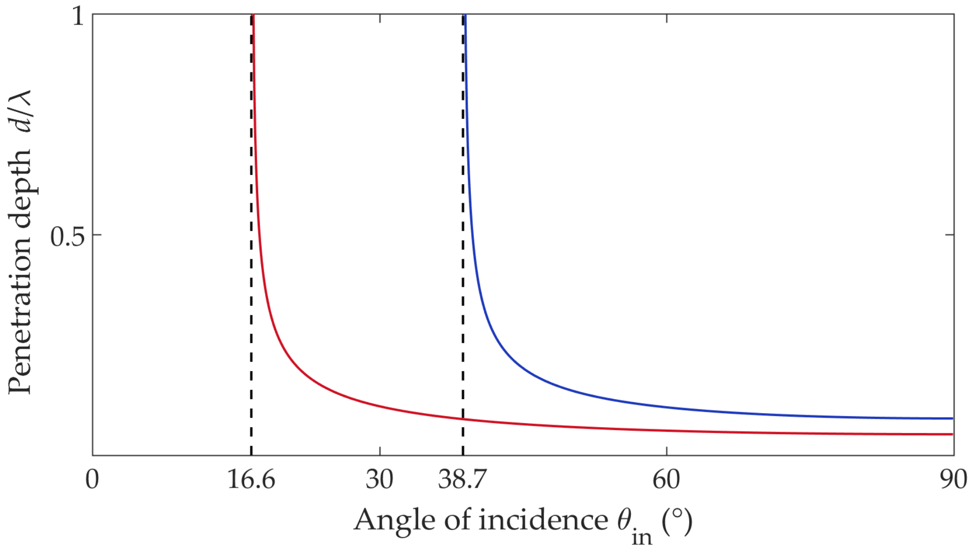

FIGURE 2.2.: Penetration depth in units of λ plotted over the incident angle θ_{in} for the transition from Si into air (red) and ZnSe into glass (blue).

the critical angle will have a huge impact on the atom light interaction within the evanescent field.

2.3. Reflectivity

After studying the transmission behavior of planewaves through a dielectric interface, this section aims to give an idea of the reflectivity R that arises due to the change in the refractive index.

Any planewave can be separated into a parallel $\boldsymbol{E}_{\text{p}}$ and perpendicular $\boldsymbol{E}_{\text{s}}$ component relative to the plane of incidence

$$\boldsymbol{E} = \boldsymbol{E}_{0,\text{p}} \cdot \exp(i\boldsymbol{k}_{\text{p}}\boldsymbol{r}) + \boldsymbol{E}_{0,\text{s}} \cdot \exp(i\boldsymbol{k}_{\text{s}}\boldsymbol{r}). \tag{2.11}$$

Further, the so far neglected magnetic field $\boldsymbol{B} = \frac{1}{c}(\boldsymbol{k} \times \boldsymbol{E})$ [16] is always perpendicular to the electric field $\boldsymbol{E}$ and the wavevector $\boldsymbol{k}$ (for $r >> \lambda$). Together with the continuity of each Cartesian components of the electromagnetic field one obtains the condition

$$(\boldsymbol{k}_{\text{in}} \times \boldsymbol{E}_{\text{in}})|_x + (\boldsymbol{k}_{\text{r}} \times \boldsymbol{E}_{\text{r}})|_x = (\boldsymbol{k}_{\text{t}} \times \boldsymbol{E}_{\text{t}})|_x, \tag{2.12}$$

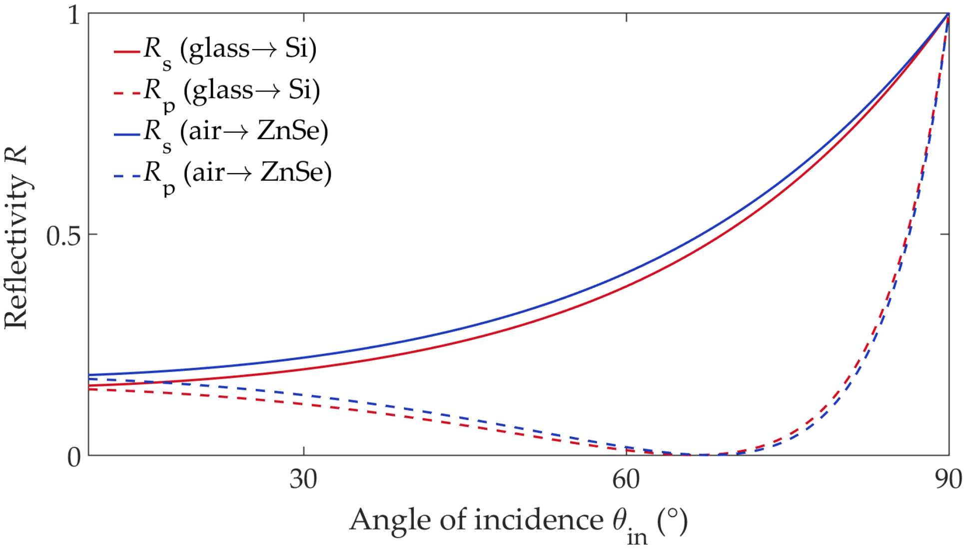

FIGURE 2.3.: Reflectivity R for perpendicular and parallel polarized light in dependence of the incident angle for the transition from glass to Si (red) and air to ZnSe (blue).

where the indices *in*, *r*, and *t* describe the incident, reflected, and transmitted wave, respectively. For the component of the electric field perpendicular to the plane of incidence (z-direction) the relation of the amplitudes reads

$$k_{\mathrm{in,y}} E^{\mathrm{in}}_{0,\mathrm{s}} + k_{\mathrm{r,y}} E^{\mathrm{r}}_{0,\mathrm{s}} = k_{\mathrm{t,y}} E^{\mathrm{t}}_{0,\mathrm{s}}. \tag{2.13}$$

Subsequently, since $k_{\mathrm{r,z}} = -k_{\mathrm{in,z}}$ and the continuity $\mathbf{E}^{\mathrm{in}}_{0,\mathrm{s}} + \mathbf{E}^{\mathrm{r}}_{0,\mathrm{s}} = \mathbf{E}^{\mathrm{t}}_{0,\mathrm{s}}$ holds true, the quotient of the reflected and incident wave can be expressed as

$$\frac{\mathbf{E}^{\mathrm{r}}_{\mathrm{s}}}{\mathbf{E}^{\mathrm{in}}_{\mathrm{s}}} = \frac{n_1 \cos(\theta_{\mathrm{in}}) - n_2 \cos(\theta_{\mathrm{t}})}{n_1 \cos(\theta_{\mathrm{in}}) + n_2 \cos(\theta_{\mathrm{t}})} =: r_{\mathrm{s}}. \tag{2.14}$$

Geometric relations like $k^{\mathrm{in}}_{\mathrm{y}} = k^{\mathrm{in}} \cos(\theta_{\mathrm{in}})$ and $k^{\mathrm{in}}_{\mathrm{y}} = k^{\mathrm{in}} \cos(\theta_{\mathrm{t}})$ were used together with Snell's law in order to convert the wavevectors into refractive indices and angles of incidence and transmission. A similar approach for the component parallel to the plane of incidence $\mathbf{E}_{\mathrm{p}}$ leads to

$$\frac{\mathbf{E}^{\mathrm{r}}_{\mathrm{p}}}{\mathbf{E}^{\mathrm{in}}_{\mathrm{p}}} = \frac{n_2 \cos(\theta_{\mathrm{in}}) - n_1 \cos(\theta_{\mathrm{t}})}{n_2 \cos(\theta_{\mathrm{in}}) + n_1 \cos(\theta_{\mathrm{t}})} =: r_{\mathrm{p}}. \tag{2.15}$$

Both Eq. (2.14) and Eq. (2.15) are called Fresnel equations of reflection. The measurable intensity I scales quadratic with the electric field $\boldsymbol{E}$, therefore, one defines the *reflectivity* $R = |r|^2$. This quantity is visualized in Fig. 2.3 for various angles of incidence for the previously mentioned materials. There is a large difference in reflection depending on the polarization of the light. One can find incident angles, so called Brewster angles, where no reflection happens for perpendicular polarized light. Equally, the transmitted amplitude can be obtained from

$$T_{\mathrm{p,s}} = 1 - R_{\mathrm{p,s}} \tag{2.16}$$

for each component separately.
The following chapter studies crucial phenomena of atoms interacting with the light field.

3. Atom Light Interaction

3.1. Two-Level Atom

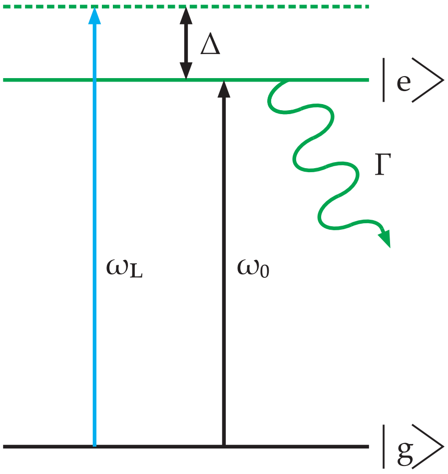

FIGURE 3.1.: Two-level scheme with ground state $|g\rangle$ and excited state $|e\rangle$ connected via the laser ω_{L} detuned from resonance ω_0 by Δ and spontaneously decaying from $|e\rangle$ to $|g\rangle$ with the decay rate Γ.

The description of light interacting with a two-level atom with ground state $|g\rangle$ and the excited state $|e\rangle$ asks for a quantum mechanic approach. All calculations and results are given in a basis of atom states $|g\rangle$ and $|e\rangle$ for a two-level atom. The individual states are orthogonal $\langle g|e\rangle = 0$. The Hamiltonian of the system contains two contributions

$$H = H_{\mathrm{A}} + H_{\mathrm{Int}}, \tag{3.1}$$

namely from the atom H_{A} and from its interaction with light H_{Int}. The atomic Hamiltonian

$$H_{\mathrm{A}} = E_{\mathrm{g}} |g\rangle \langle g| + E_{\mathrm{e}} |e\rangle \langle e| = \hbar\omega_0 |e\rangle \langle e| \tag{3.2}$$

is reduced to a contribution of the excited state $|e\rangle \langle e|$ when the origin (lowest energy level) is chosen to be at the ground state $|g\rangle$. In that case E_{g} stands for the energy separation of the ground state to zero energy and $E_\mathrm{e} = \hbar\omega_0$ for the level spacing between ground and excited state. The contribution of the radiative field H_R can be neglected for cases of classical light. However, the atom light interaction has to be included via

$$H_\mathrm{Int} = -\boldsymbol{dE}. \tag{3.3}$$

This Hamiltonian results from the electric dipole approximation where the wavelength λ of the electromagnetic wave is estimated to be much larger than the observed system (in that case one atom). This leads to a linear approximation of the spatial distribution of the electromagnetic field

$$\exp(i\boldsymbol{kr}) \approx 1 + i\boldsymbol{kr} \approx 1, \quad \text{for} \quad \boldsymbol{kr} \approx \frac{2\pi a_0}{\lambda} \ll 1 \tag{3.4}$$

leaving behind only the time evolution. Thus, one only observes the (electric) *dipole allowed* transitions (zero order). The dipole matrix transition element from state i to j is then given by $\boldsymbol{d}_{ij} = e\,\langle i|\,\boldsymbol{r}\,|j\rangle$ and is included in the Rabi frequency Ω as follows

$$\Omega = \frac{\boldsymbol{d}_\mathrm{ij}\boldsymbol{E}}{\hbar}. \tag{3.5}$$

Before deriving the main features of this system one changes the time frame of the light frequency ω_L in order to simplify the following calculations and results. This is accomplished by the application of the *Rotating Wave Approximation* (RWA).

3.1.1. Rotating Wave Approximation

The full representation of the electric field shows the dependency on the laser frequency ω_L

$$H = \hbar \begin{pmatrix} 0 & -\frac{\boldsymbol{d}_\mathrm{ge}}{2}(E_0 e^{-iw_\mathrm{L}t} + E_0^* e^{(+iw_\mathrm{L}t)}) \\ -\frac{\boldsymbol{d}_\mathrm{eg}}{2}(E_0 e^{-iw_\mathrm{L}t} + E_0^* e^{(+iw_\mathrm{L}t)}) & \omega_0 \end{pmatrix}. \tag{3.6}$$

Note that a parallel orientation of the dipole and the electric field with $\boldsymbol{d}_{ij}\boldsymbol{E} = d_{ij}E$ was chosen without loss of generality. Hence, the system evolves in time with the frequencies ω_L from the point of view of a resting observer. However, one only expects effects at resonance frequency ω_0. Therefore, it is handy to switch into a rotating basis with frequency ω_L. This approach is valid for weak atom light interaction [17]. The unitary transformation matrix

$$U = \begin{pmatrix} 1 & 0 \\ 0 & \exp(-i\omega_\mathrm{L}t) \end{pmatrix} \tag{3.7}$$

allows one to switch into the rotating frame. The new Hamiltonian in the rotating basis can be calculated with

$$\tilde{H} = U^\dagger H U - i\hbar U^\dagger \partial_{\mathrm{t}} U. \tag{3.8}$$

Using Eq. 3.6 together with Eq. 3.8 one obtains

$$\tilde{H} = \hbar \begin{pmatrix} 0 & -\frac{\boldsymbol{d}_{\mathrm{ge}}}{2}(E_0 + E_0^* e^{+2iw_{\mathrm{L}}t)}) \\ -\frac{\boldsymbol{d}_{\mathrm{eg}}}{2}(E_0 e^{-2iw_{\mathrm{L}}t} + E_0^*) & \omega_0 - \omega_{\mathrm{L}} \end{pmatrix}. \tag{3.9}$$

The detuning $\Delta = \omega_{\mathrm{L}} - \omega_0$ is visualized in Fig. 3.1. Since the fast oscillating terms $2\omega_{\mathrm{L}}$ evolve on a much shorter time scale than the atomic resonance ω_0 one can neglect those terms on a time average. What remains is the full Hamiltonian of the two-level system

$$\tilde{H} = \hbar \begin{pmatrix} 0 & \frac{\Omega_0}{2} \\ \frac{\Omega_0^*}{2} & -\Delta \end{pmatrix} \tag{3.10}$$

with the time independent Rabi frequency $\Omega_0 = \frac{\boldsymbol{d}_{ij}\boldsymbol{E}_0}{\hbar}$.The last missing piece is the spontaneous decay rate Γ from the excited state to the ground state which arises from the uncertainty principle. Those decay rates and other decoherence factors can be easily applied by using the density matrix formalism.

3.1.2. Density Matrix Formalism

This section aims to derive the optical Bloch equations that fully describe the two-level atom. A useful tool is the density matrix operator

$$\rho = \sum_i p_i \left|\psi_i\right\rangle \left\langle\psi_i\right|. \tag{3.11}$$

Here, $0 \leq p_i \leq 1$ describes the probability to find the system in a pure state $|\psi_i\rangle$. The latter span a full orthonormal basis of a (clearly defined) Hilbert space. Without discussing the details [18] of its properties we directly introduce its application for any n level atomic system. For a two-level atom,

$$\rho = \begin{pmatrix} \rho_{11} & \cdots & \rho_{1n} \\ \vdots & \ddots & \\ \rho_{n1} & & \rho_{nn} \end{pmatrix} = \begin{pmatrix} \rho_{gg} & \rho_{ge} \\ \rho_{eg} & \rho_{ee} \end{pmatrix} \tag{3.12}$$

describes the population of the ground and excited state in the diagonal elements with $\mathrm{Tr}(\rho^2) \leq 1$ and the coherence in its off-diagonal elements which connects two levels, and accounts for interference effects. In order to include decoherence processes like spontaneous emission one introduces the Lindblad master equation [19]

$$i\hbar\dot{\rho} = [H,\rho] + i\hbar L_{\mathrm{D}} = [H,\rho] + 2i\hbar \sum_{ge} (V_{ge}\rho V_{ge}^{\dagger} - \frac{1}{2}\{V_{ge}^{\dagger}V_{ge}, \rho\}) \tag{3.13}$$

with the Lindblad operator defined as L_{D}. Applied to our two-level atom, $V_{ge} = \sqrt{\frac{\Gamma_{eg}}{2}}\,|g\rangle\,\langle e|$ represents the transition operator from state $|g\rangle$ to $|e\rangle$.
The first component of L_{D} reads

$$\begin{aligned} V_{ge}\rho V_{ge}^{\dagger} &= \sqrt{\frac{\Gamma_{eg}}{2}} V_{ge}(\rho\,|e\rangle\,\langle g|) \\ &= \sqrt{\frac{\Gamma_{eg}}{2}} V_{ge}(\rho_{ge}\,|g\rangle\,\langle g| + \rho_{ee}\,|e\rangle\,\langle g|) \\ &= \frac{\Gamma_{eg}}{2}\rho_{ee}\,|g\rangle\,\langle g|\,, \end{aligned} \tag{3.14}$$

while the second component yields

$$\begin{aligned} V_{ge}^{\dagger}V_{ge}\rho + \rho V_{ge}^{\dagger}V_{ge} &= \sqrt{\frac{\Gamma_{eg}}{2}} V_{ge}^{\dagger}(\rho_{eg}\,|g\rangle\,\langle g| + \rho_{ee}\,|g\rangle\,\langle e|) + \frac{\Gamma_{eg}}{2}\rho\,|e\rangle\,\langle e| \\ &= \frac{\Gamma_{eg}}{2}(\rho_{eg}\,|e\rangle\,\langle g| + \rho_{ee}\,|e\rangle\,\langle e| + \rho_{ge}\,|g\rangle\,\langle e| + \rho_{ee}\,|e\rangle\,\langle e|). \end{aligned} \tag{3.15}$$

Altogether, one obtains

$$L_{\mathrm{D}} = \Gamma_{eg}\begin{pmatrix} \rho_{ee} & \frac{-\rho_{ge}}{2} \\ \frac{-\rho_{eg}}{2} & -\rho_{ee} \end{pmatrix}. \tag{3.16}$$

In the off-diagonal elements one usually substitutes $\frac{\Gamma_{eg}}{2}$ with $\Gamma_{\mathrm{dec}} = \Gamma_{\mathrm{q}} + \frac{\Gamma_{eg}}{2}$ to include other decoherence effects Γ_{q}. Before evolving the Hamiltonian in time, one also has to switch from resting to rotating basis in the density matrix formalism as follows

$$\sigma = \begin{pmatrix} \sigma_{gg} & \sigma_{ge} \\ \sigma_{eg} & \sigma_{ee} \end{pmatrix} = \begin{pmatrix} \rho_{gg} & \rho_{ge}e^{+i\omega_{\mathrm{L}}t} \\ \rho_{eg}e^{-i\omega_{\mathrm{L}}t} & \rho_{ee} \end{pmatrix}. \tag{3.17}$$

This does not affect the appearance of the Lindblad equation. In terms of the rotated frame one can finally write the differential equations for every component of the master equation (Eq. 3.13)

$$\dot{\sigma}_{gg} = -\frac{i}{2}(\Omega_0 \sigma_{eg} - \Omega_0^* \sigma_{ge}) + \Gamma_{eg}\sigma_{ee} \tag{3.18a}$$

$$\dot{\sigma}_{ge} = -\frac{i}{2}(\Omega_0 \sigma_{ee} - \Omega_0 \sigma_{gg}) - \left(\frac{\Gamma_{eg}}{2} + i\Delta\right)\sigma_{ge} \tag{3.18b}$$

$$\dot{\sigma}_{eg} = +\frac{i}{2}(\Omega_0^* \sigma_{ee} - \Omega_0^* \sigma_{gg}) - \left(\frac{\Gamma_{eg}}{2} - i\Delta\right)\sigma_{eg} \tag{3.18c}$$

$$\dot{\sigma}_{ee} = +\frac{i}{2}(\Omega_0 \sigma_{eg} - \Omega_0^* \sigma_{ge}) - \Gamma_{eg}\sigma_{ee}. \tag{3.18d}$$

The obtained equations are the so called *optical Bloch equations* which fully describe the two-level system. Actually, there are only three independent equations since $\dot{\sigma}_{ge} = \dot{\sigma}_{eg}^*$. Since this experiment uses continuous wave (CW-) lasers only, one is interested in the steady state solution ($\dot{\sigma} = 0$) of the master equation rather than its time evolution. The only starting condition is $\langle \rho_{gg} \rangle \overset{!}{=} 1$. After solving the steady state equations we are interested in real measurable properties of the two-level atom, so the next section defines and studies the observable called *susceptibility*.

3.1.3. Dielectric Susceptibility

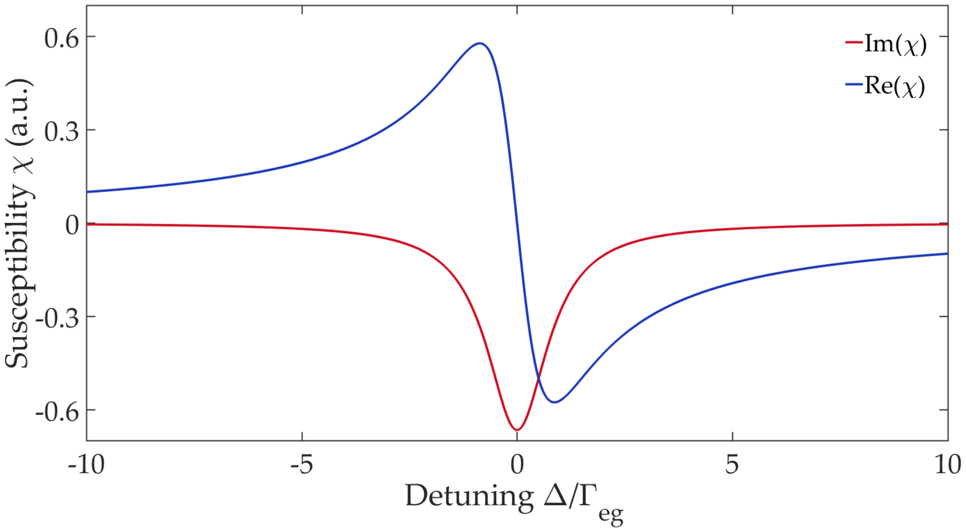

FIGURE 3.2.: Real (blue) and imaginary (red) part of the dielectric susceptibility χ over detuning Δ for $\Omega = \Gamma_{eg}$.

The polarization (density) of an atomic medium is directly related to the electric field

$$\boldsymbol{P} = \epsilon_0 \chi \boldsymbol{E}. \tag{3.19}$$

Here one can clearly see the interaction between light and media coupled via the susceptibility χ. Generally, χ is a tensor that connects each polarization of the medium with the corresponding electric field which does not have to be parallel. However, assuming a homogeneous isotropic medium with $\boldsymbol{P}||\boldsymbol{E}$ the susceptibility can be reduced to its diagonal elements, becoming a scalar effectively. The polarization is given by the sum over all microscopic dipoles in the medium

$$\boldsymbol{P} = \frac{1}{V}\sum_i -e\boldsymbol{r}_\mathrm{i} = -ne\boldsymbol{r}_\mathrm{res}. \tag{3.20}$$

The last equality sign combines the sum over N particles and defines the density $n = \frac{N}{V}$ with the resulting polarization axis $\boldsymbol{r}_\mathrm{res}$. Thus, one has to calculate the expectation value of the dipole operator. The density matrix formalism allows one to write

$$P = n\left\langle -er\right\rangle = n\mathrm{Tr}(d\sigma) = n(d_{ge}\sigma_{ge}e^{-i\omega_\mathrm{L}t} + d_{eg}\rho_{eg}e^{+i\rho_\mathrm{L}t}). \tag{3.21}$$

Comparing the prefactors with Eq. 3.19 one directly obtains together with Eq. 3.5

$$\chi = \frac{-nd_{eg}^2}{\epsilon_0\hbar\Omega_0}\sigma_{ge} = \frac{-nd_{eg}^2}{\epsilon_0\hbar\Omega_0}\frac{\Delta + i\frac{\Gamma_{eg}}{2}}{\Delta^2 + \frac{\Gamma_{eg}^2}{4} + \frac{\Omega_0^2}{2}} \tag{3.22}$$

an explicit expression for the susceptibility of a two-level atom which contains all quantities describing the atom light interaction. The line shape of this quantity is shown in Fig. 3.2 for the real (blue) and the imaginary (red) part separately. The

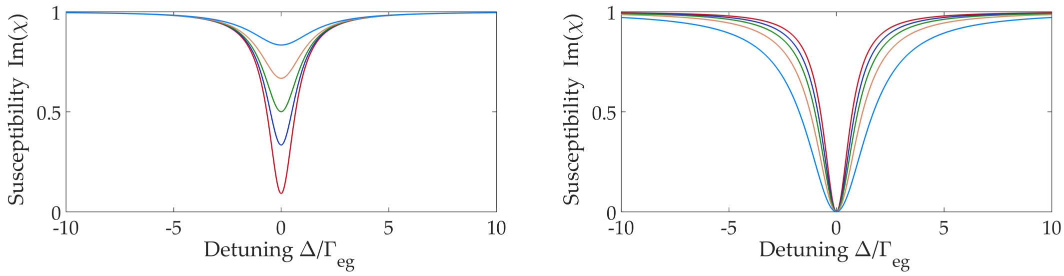

FIGURE 3.3.: Imaginary part of the susceptibility for increasing quotient $\frac{I}{I_\mathrm{sat}} = 0.1...10$ from red to blue. The amplitude decreases with increasing quotient (left), whereas the width increases in the normalized spectrum (right). Each color stands for the same parameters in both figures.

latter is usually referred to an absorptive feature while $\mathrm{Re}(\chi)$ exhibits a dispersive line shape. Focusing on the absorptive feature, $\mathrm{Im}(\chi)$ has a typical Lorentzian shape with a **f**ull **w**idth at **h**alf **m**aximum (FWHM) $\Delta\omega_{\mathrm{L}}$ of

$$\Delta\omega_{\mathrm{L}} = \Gamma_{eg}\sqrt{1+\frac{2\Omega_0^2}{\Gamma_{eg}^2}} = \Gamma_{eg}\sqrt{1+\frac{I}{I_{\mathrm{sat}}}}. \tag{3.23}$$

Typically, the quotient of Rabi frequency over natural linewidth Γ_{eg} can be expressed as intensity over saturation intensity. The latter defines when the absorption line starts to broaden significantly. Simultaneously, the amplitude of the signal decreases. Compare with Fig. 3.3 to see both effects on the susceptibility. Note that if one actually uses an overall decoherence rate Γ_{dec} in the Lindblad operator this will appear in the width as a sum over all broadening effects. Those effects that influence each atom equally contribute to homogeneous line broadening and can be added up. Besides the natural line width Γ_{eg} and the power broadening from $\frac{I}{I_{\mathrm{sat}}}$ one could expect broadening effects originating from collision, either with walls or with other atoms at high densities n.

3.2. Absorption of Light

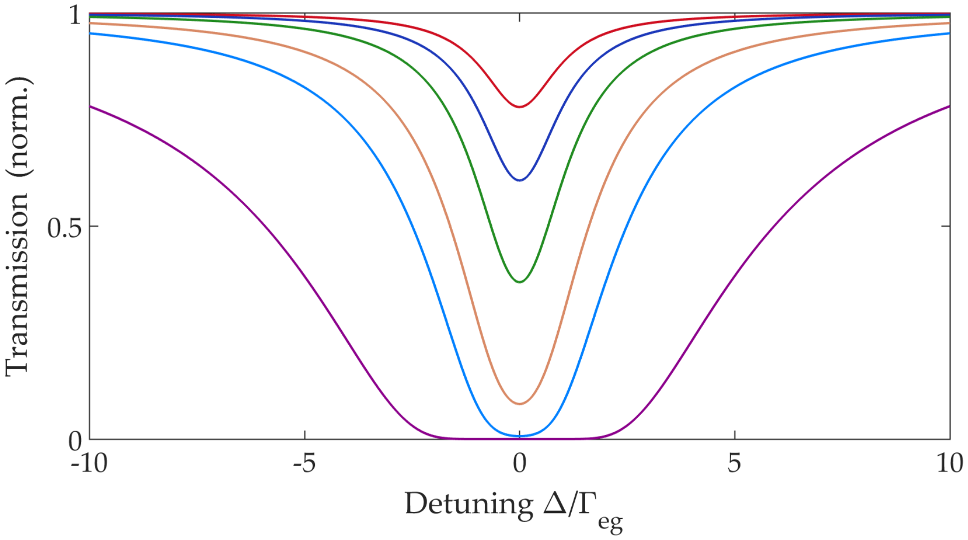

Figure 3.4.: Transmission from the collective transfer function T for increasing density n from red to purple.

The derived expression for the susceptibility so far is only valid for weak probe fields and a homogeneous medium corresponding to N atoms equally excited by an electromagnetic field. However, this does not resemble a real experiment since for a dense medium, atoms further away from the light source have a smaller probability to interact with a photon than atoms close to it. The collective response of the medium is then given by the transfer function [20]

$$T = \exp\left(-\frac{1}{2} i k_0 z \chi\right). \tag{3.24}$$

This resembles Beer-Lambert's Law with an absorption coefficient $\gamma = i k_0 \chi$. Since the derived susceptibility is only given for *linear* response of the medium, the exponent could be understood as a first oder approximation of the refractive index which appears in the magnitude of the wave vector ($k = n k_0$)

$$n = \sqrt{1+\chi} \approx 1 + \frac{\chi}{2} + \mathcal{O}(\chi^2). \tag{3.25}$$

Here we assumed that the medium has no magnetic response. Thus, the Maxwell equations give

$$n = \sqrt{\epsilon_\mathrm{r}\mu_\mathrm{r}} \approx \sqrt{\epsilon_\mathrm{r}} = \sqrt{1+\chi} \tag{3.26}$$

with the magnetic permeability μ_r.
The importance of Eq. 3.24 can be seen in Fig. 3.4. For high enough densities, the transmission drops completely to zero making the medium opaque around resonance ω_0. To summarize, the transfer function T allows for a precise description of an atomic ensemble interacting with light. It is not limited to a two-level system only as one will see later on. Also this expression is used to fit and simulate all following transmission (absorption) spectra.
Another contribution to the spectrum is provided by the motion of atoms which gives rise to the Doppler broadening.

3.3. Atoms in Motion

3.3.1. Transit Time Broadening

So far the motion of atoms was neglected. However, there are crucial effects originating from atoms moving at *different* velocities and directions. Since the velocity and direction is different from atom to atom this kind of broadening is referred to as inhomogeneous broadening.
The first effect, called transit time, emerges as follows: Since the light field has a finite size, it only talks to atoms flying through the field. If this spatial interaction region is smaller than the distance traveled by the atom while being excited, transit time broadening is clearly noticeable in the linewidth. Usually this condition is easily achieved with evanescent fields due to the fast exponential decay of the field. For smaller interaction regions or faster atoms transit time leads to increased broadening of the spectrum.

3.3.2. Doppler Broadening

Considering a laser beam, transit time effects are mainly dominant for atoms moving perpendicular to the laser. In case of propagation along or towards the laser, the Doppler effect plays an important role.
For an atom moving towards (-) or away (+) from the laser, the resonance frequency ω_0 has to be adjusted by

$$\omega = \omega_0 \pm k_\mathrm{x} v_\mathrm{x} \cos(\alpha). \tag{3.27}$$

Without loss of generality we only consider one component of the wavevector k_x and the corresponding velocity of the atom v_x, while α describes the relative angle between the moving direction of photon and atom. For example, an atom moving perpendicular to the laser experiences no Doppler effect. For the further calculations

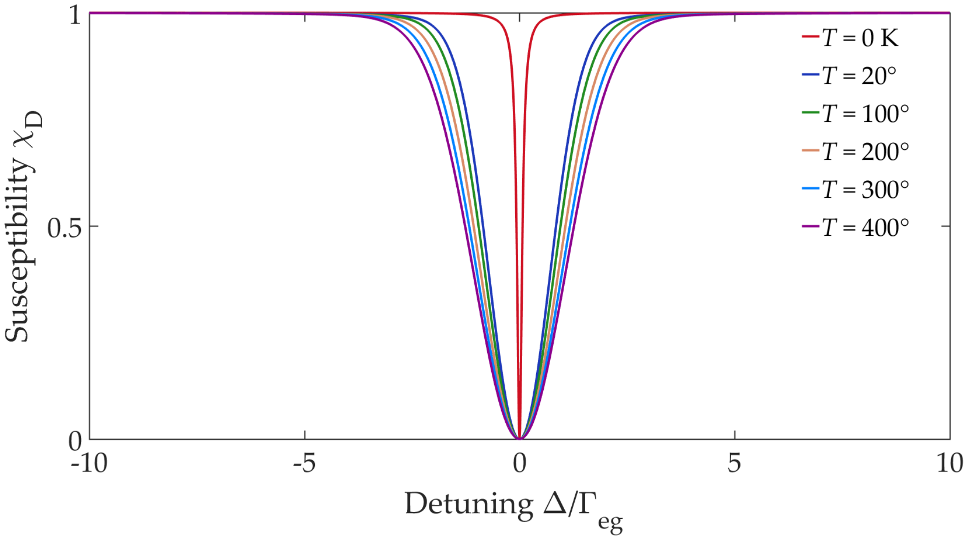

FIGURE 3.5.: Susceptibility for no Doppler broadened (red) and for a vapor from 20°C to 400°C.

we only focus on counter-propagating atoms and photons, so $\omega = \omega_0 - k_x v_x$. Typically, each component of the velocity in a thermal vapor corresponds to the normal distribution

$$P(v_x) = P_0 \exp\left(\frac{-E_{\text{kin}}}{E_{\text{thermal}}}\right) = P_0 \exp\left(\frac{-mv_x^2}{2k_B T}\right) \tag{3.28}$$

with kinetic energy E_{kin} as function of mass m and velocity of the atom and normalization factor P_0. The thermal energy E_{thermal} is given by the product of Boltzmann constant k_B and temperature T. From Eq. 3.27 one can define $v_x = \frac{c}{\omega_0}(\omega - \omega_0)$. With this substitution we arrive at the frequency dependent distribution

$$P(\omega) = P_0 \exp\left(\frac{-mc^2(\omega - \omega_0)^2}{2\omega_0^2 k_B T}\right). \tag{3.29}$$

The distribution has a Gaussian shape with a FWHM of

$$\omega_D = \frac{\omega_0}{c}\sqrt{\frac{8\ln(2)k_B T}{m}} = 2\sqrt{2\ln(2)}\sigma_D. \tag{3.30}$$

Note that the FWHM is given by $2\sqrt{2\ln(2)}$ times the standard deviation σ_D for a Gaussian (or normal) distribution. Thus, the Doppler broadening scales with the square root of the temperature.

In order to include this inhomogeneous broadening mechanism into the susceptibility, one has to weight each detuning of χ with the normal distribution. This can be done by calculating the convolution

$$\chi_{\mathrm{D}} = (P * \chi)(\Delta) = \int_{-\infty}^{\infty} P(v)\chi(\Delta - kv)dv. \tag{3.31}$$

This broadening effect in comparison to atoms moving only perpendicular to the laser (so $v_{\mathrm{x}} = 0$) or at absolute zero temperature (red) is visualized in Fig. 3.5. The lineshape of χ_{D} is a mixture of Lorentzian and Gaussian profile and is called *Voigt* profile. Depending on which broadening, homogeneous or inhomogeneous, contributes most to the susceptibility, one can approximate the lineshape with a Gaussian or Lorentzian, only. It is not possible to give an analytic expression for χ_{D} without approximation.

4. Experimental Setup

4.1. Telecom Laser

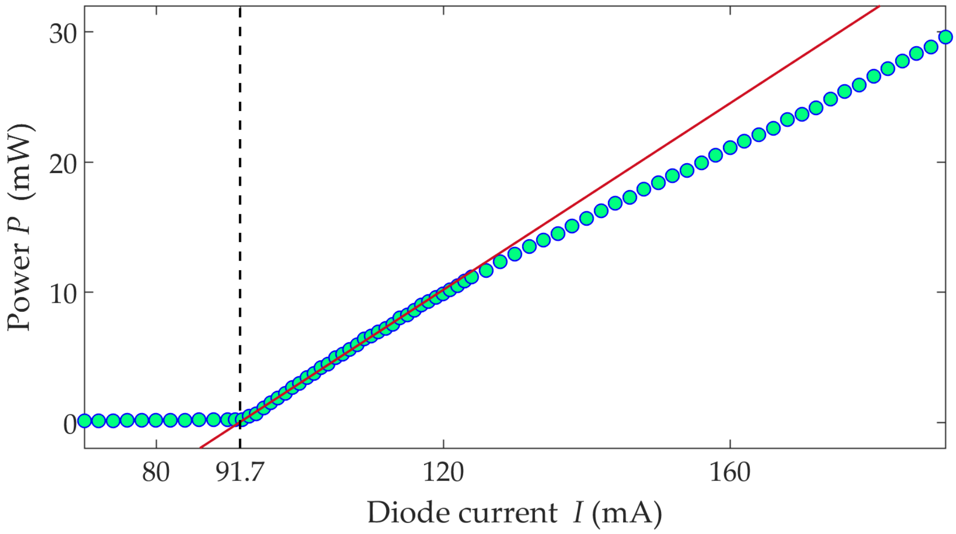

FIGURE 4.1.: Lasing transition of the telecom diode running at a wavelength of 1529 nm and a temperature of 25°C with linear interpolation (red) of the lasing threshold (vertical line).

A new laser setup was established for Rb excitation at the telecom (telecommunication) wavelengths, in particular for the S (1460-1530 nm) and C (1530-1565 nm) band. The targeted wavelength of 1529.37 nm corresponds to the upper end of the S band and extends to the lower bound of the C band. The laser diode (#LD-1550-0050-AR-2) provided by Toptica features an emission spectrum from 1520 nm to 1565 nm with a maximum power of 50 mW at 1550 nm.

The diode is inserted into an already existing Toptica DL pro laser head together with a suitable new optical isolator. The diode is in a Littrow configuration with an external resonator, which consists of the grating surface and the facet of the laser diode. Via screws in the diode holder, one can adjust the position of the diode and by that tune the resonator. The main goal is to achieve maximum gain for the

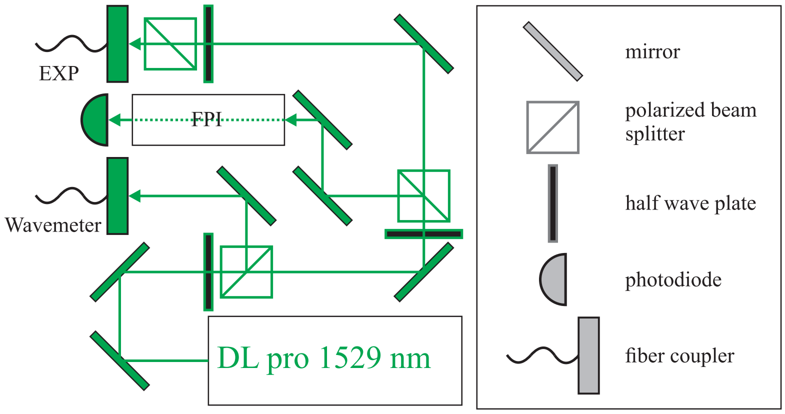

Figure 4.2.: Telecom wavelength laser setup with all optical components used for the experiment. The main features are the Fabry-Pérot cavity for frequency scaling and the wavemeter for wavelength determination with 0.01 nm accuracy.

desired wavelength. Therefore, one changes the grating angle relative to the diode facet in tiny steps while adjusting the diode position with the screws. As soon as lasing (significant power increase) is visible, one optimizes the output power via the screws only. By monitoring the wavelength on a wavemeter, one can find the maximum gain for the targeted wavelength.

The grating is in contact with a piezo element for frequency scanning. The temperature control for the diode housing is set to 25°C and the limited diode current is 195 mA, resulting in a peak power of 30 mW right after the laser head. However, the maximum threshold for the diode current is 350 mA, so the maximum power is 50 mW.

A characterization of the lasing power is given in Fig. 4.1. The linear fit in red is used to determine the lasing threshold (dashed line) of ≈ 92 mA. Note that the lasing threshold rises from 1550 nm to 1529 nm starting from ≈ 75 mA.

The whole laser system is powered and controlled by a DC110, also from Toptica. Mode-hope free frequency detuning up to 10 GHz is possible via the scan control unit (SC110). The scan repetition rate (or scan frequency) is set to ≈ 7.7 Hz for all measurements. Fig. 4.1 was measured including the isolator. The transmission loss caused by the optical isolator is 8.6%.

The telecom laser setup is sketched in Fig. 4.2. The (transversal) mode leaving the laser head highly deviates from the desired Gaussian (TEM 00) shape. However, after roughly 2 m of propagation a purely Gaussian mode remains with no noticeable divergence along the remaining beam path. After that, no further beam shaping is necessary.

The laser is sent into a wavemeter (Advantest TQ8235) for precise wavelength

determination and into a home-built Fabry-Pérot cavity with 1820 MHz free spectral range that provides a calibrated frequency axis for all measurements scanning the telecom laser. Note that all half-waveplates that were used are suited for a wavelength of 1550 nm. Only Thorlabs zero order half waveplates with a retardance of $\approx 0.51\lambda$ (at 1529 nm) followed by **p**olarizing **b**eam **s**plitters (PBS) were used. Thus, generation of elliptically (or circularly) polarized light is kept minimal.
The PBS just before the fiber can be rotated in such a way that the transmitted polarization matches the axis of the single mode polarization maintaining fiber. Up to 80 % coupling efficiency can be achieved, which is a sign for a Gaussian beam profile.

4.2. Wafer Cell Fabrication

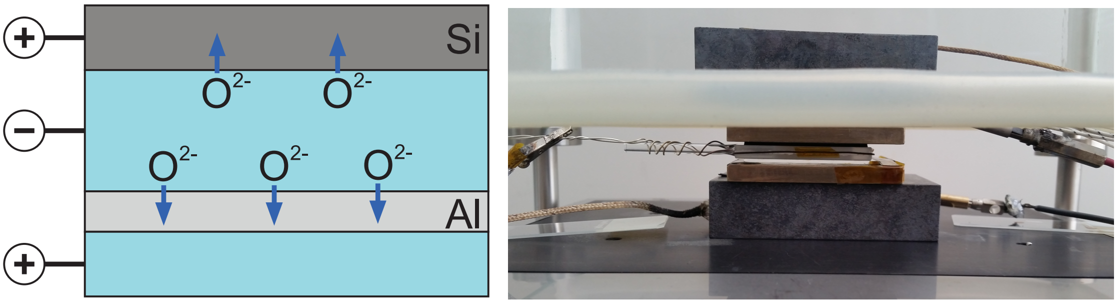

Figure 4.3.: Left: Bonding schematics including all layers. Both windows, silicon and glass, are connected to a positive pole while the glass frame is connected to the negative pole. The negative oxygen atoms in the depletion region at the boundary to the windows recombine with Si and Al, respectively. Right: Photograph of the cell while the bonding process. The upper and lower copper blocks are connected to the corresponding pole and also heat the cell. The wire wrapped around the glass frame provides the negative pole.

This section describes the fabrication of the cell that will be studied in chapter six. All other cells were already provided for the experiment and are mainly commercial cells filled with rubidium.
A glass frame (50x20x5 mm) with attached glass tube is sandwiched between two windows. One is made of glass and the other one is made of pure silicon. Anodic bonding ensures hermetic sealing of the interior. Borosilicate glass (81 % SiO_2, 13 % B_2O_3, 4 % Na_2O/K_2O and 2 % Al_2O_3 [21]) was chosen due to the high alkali ion concentration. That ion concentration is crucial for anodic bonding of the glass.
A detailed study to the fabrication of our home-built cells can be found in [22]. Here, only the basic principle will be explained. Heating the glass up to 300°C

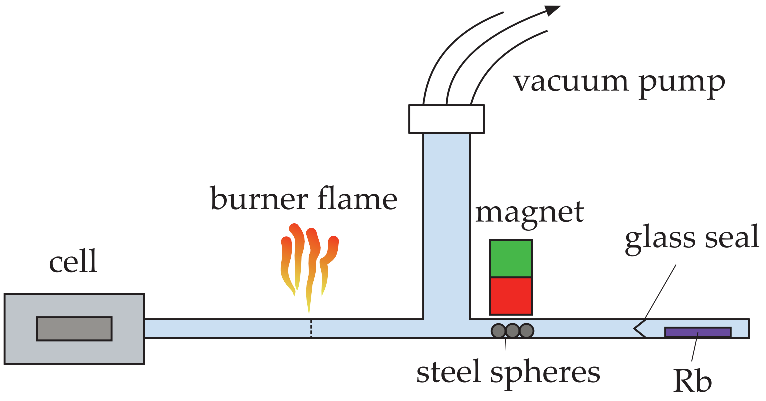

FIGURE 4.4.: Filling station for the vapor cell (top view). The rubidium reservoir and the cell are attached to a vacuum pump. The steel spheres together with the magnet can break the seal and transfer Rb to the vapor cell. Afterwards, the cell with the Rb reservoir is sealed with a burner.

ensures free Na^+ (and K^+) ions diffusion. Applying a potential of around 1.5 kV for this particular cell causes the positive ions to move towards the negative pole. Hence, a negatively charged depletion region with O^{2-} ions remains. Consequently, one can use this depletion region to induce recombination of positively charged ions from a different material. The schematics as well as the picture of the bonding process can be seen in Fig. 4.3. By applying a positive potential to the Si window and a negative potential to the glass frame, one induces recombination of Si and O^{2-} to SiO_2 which bonds the window to the frame. Simultaneously, the bonding of the glass window from the other side is possible. However, since it is impossible to bond glass to glass, an aluminum layer was deposited on the glass window. By applying a positive potential to the other window as well, one forces recombination of Al from the glass window with O^{2-} from the frame which forms the bonding Al_2O_3 layer. The result is a hermetic sealed cell with Si and glass window. After applying the voltage, one monitors the current through the electrodes. A clear exponential decay indicates the recombination process and ensures a successful bonding.

The next step is the filling of the cell with rubidium. In order to evacuate the interior, both the cell and the rubidium reservoir are attached to a vacuum pump, as can be seen in Fig. 4.4. After the desired pressure of $< 3 \cdot 10^{-7}$ mbar is reached, the inserted steel spheres are used to break the glass seal. The heated rubidium liquid can be poured into the tube just before the cell interior. Afterwards, the cell and the Rb reservoir are melted off and sealed at the dashed line in Fig. 4.4 with a burner.

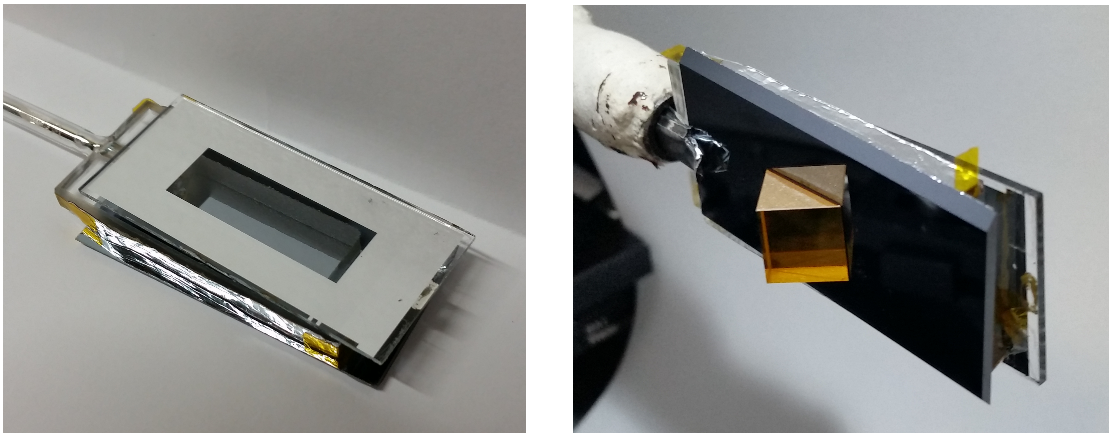

Figure 4.5.: Photographs of the fabricated wafer cell. Left: Glass window of the cell. Right: Si window with attached ZnSe prism.

The final step is performed by adding the zinc selenide (ZnSe) prism to the Si surface. This is simply done by gluing the prism to the Si window with an epoxy (EPO-TEK 301-2) [23]. The finished wafer cell is depicted in Fig. 4.5.

4.3. Evanescent Spectroscopy and Reference

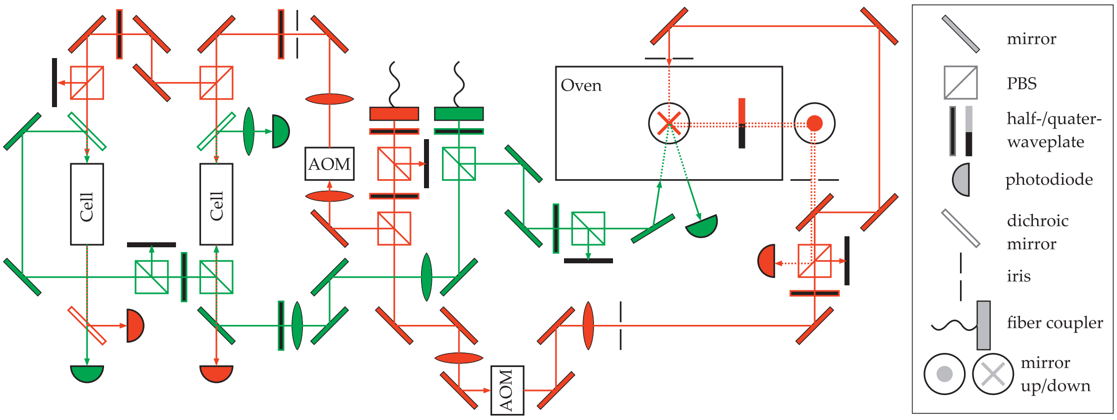

Figure 4.6.: Spectroscopy setup for interaction of evanescent probe light with an atomic vapor. The color coding follows Fig. 4.2. Additionally, the modulated 780 nm laser is represented in red. Main features of the setup are the two reference cells and the wafer cell inside the oven.

The spectroscopy setup is depicted in Fig. 4.6.
Both (reference) cells are identical regarding size and heating. They consist of a 10 cm glass cylinder with a drop of Rb inside. The cylinder is wrapped by a heating foil. The top and bottom of the cylinder is heated with a piece of copper from above to prevent condensation of Rb on those windows. One cell is used for counter-propagating excitation, and the other one is used for the co-propagating scheme.
Both lasers are detected on photo diodes after propagating through the cells. The telecom laser shows a two-photon spectrum which will be discussed in the next section, while the 780 nm laser is used to determine the optical density inside the cell. In order to maximize the signal from the reference cells, both lasers are extended in their beam diameter after leaving the fiber. Also, to filter out non-linear polarizations, both lasers pass a PBS before entering the cell. The overlapping beams are separated with dichroic mirrors. Additionally, the 780 nm laser is modulated using an **a**cousto-**o**ptic **m**odulator (AOM) which improves the signal-to-noise ratio when combined with a Lock-In amplifier.
Following the path on the right in Fig. 4.6, both beams eventually enter the oven. There are two paths the 780 nm laser can go: the first one enters the oven from the back, whereas the second path is from above. The 'dot' denotes propagation out of plane, while the cross stands for the beam traveling into the plane. A quarter-waveplates is used to measure the optical density of the cell in the oven by detecting the reflected 780 nm beam on a photo diode. For the fabricated cell,

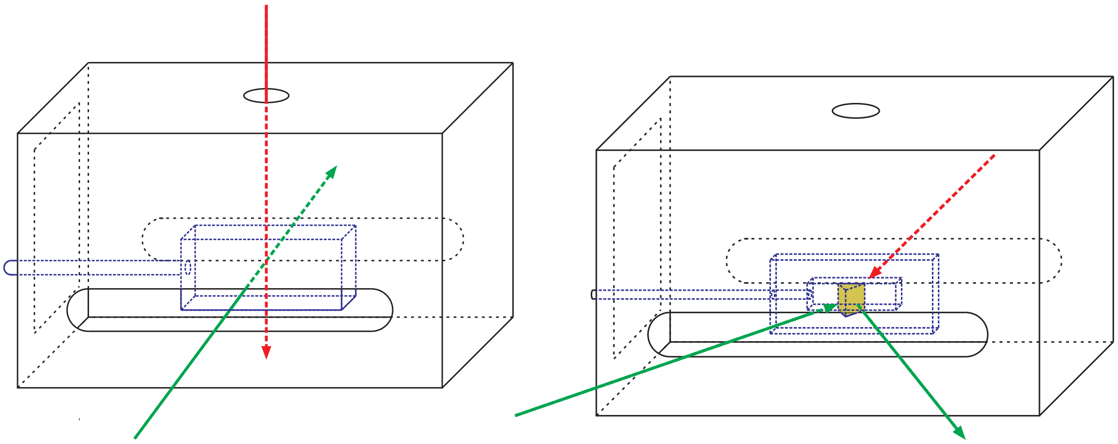

FIGURE 4.7.: Left: Perpendicular excitation scheme with commercial glass cell. Right: Evanescent excitation scheme with home-built wafer cell. Red arrows represent the pump beam (780 nm) whereas green arrows stand for the probe beam (1529 nm).

the path leading behind the oven is selected. In other cases, a commercial glass cell (without silicon and prism) was studied for excitations with perpendicular pump (780 nm) and probe (1529 nm) beam excitation. For those measurements, the excitation from above is used. The green photo diode in front of the oven is located behind the oven for that case.

The wafer cell is mounted inside the *reservoir heater*, which consists of a copper tube wrapped with heating wire and thermal glue (Cerastil). Further, the reservoir heater is mounted on a precision xyz-stage allowing position fine tuning on a nm scale. This stage is mounted on a home-built translation stage enabling a displacement of about 10 cm. This allows a compact arrangement of the oven and the optics by moving the cell in and out of the oven (instead of moving the whole oven).

The oven itself consist of a copper block with six holes for heating cartridges, allowing for separate temperature control for reservoir and oven. This block is fixed and surrounded by a larger TECAPEEK shell for further thermal isolation. The whole oven is wrapped in aluminum foil for thermal isolation leaving only slits open for laser excitation. Note that the hole on top is additionally covered with three layers of glass. This precautionary measure was implemented to prevent cold spots on top of the cell, since the hot air inside the oven can easily escape through that hole. Both perpendicular and evanescent excitation schemes can be seen in Fig. 4.7 left and right, respectively. A detailed discussion of both excitations can be found in the following chapters.

Fig. 4.8 visualizes the cross section through the cell with all layers. The probe

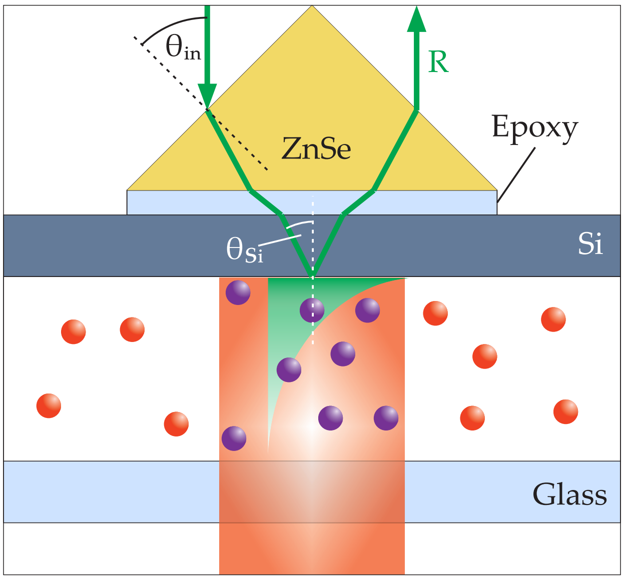

Figure 4.8.: Cross section of the wafer cell with including all media. The 1529 nm probe beam is shown in green. Its evanescent decay at the Si→vapor interface is marked as a green exponential curve. The spheres represent rubidium atoms (red). Atoms within the red pump laser at 780 nm are excited to 5P (purple).

beam is coupled in with a prism in order to reach total reflection at the Si→vapor boundary. ZnSe was chosen due to the high refractive index difference between Si and vapor. To reach the necessary angle of incidence one needs to come as close as possible to the refractive index 3.5. ZnSe offers a refractive index of 2.45 with moderate absorption ($\approx 25\%$) of 1529 nm light. The case for total reflection is depicted in Fig. 4.8. The probe laser decays exponentially into the vapor and interacts with the atoms. The reflected beam 'R' leaving the prism carries information of the atomic vapor.

The pump laser coming through the glass window excites the atoms (red) to the 5P state (purple). Only 'purple' atoms within the evanescent field contribute to the two photon signal.

In the following chapters the 'angle of incidence' θ_{in} refers to the incident angle into the prism θ_{in}. Zero degree incidence is the normal on the surface where the probe hits the prism. In Fig. 4.8 for example, the angle of incidence into the prism is $+45°$.

A different usage of the expression 'angle of incidence' refers to the angle θ_{Si} into the Si→vapor boundary. While the former can vary from 0° to 90°, the latter spans only a small range due to the large change in refractive indices.

5. Doppler-free Spectroscopy at Telecom Wavelength

In this chapter measurements from the reference cells are presented. The observed $4D_{5/2}$ spectra are fitted and characterized. The saturation intensity is derived from the power broadening measurements. The Autler-Townes effect allows precises determination of the pump Rabi frequency. Differences for co- and counter-propagating laser beams are highlighted. In comparison to the previous spectra, the spectrum of the ^{87}Rb isotope is presented at the end of this chapter.

5.1. Excitation Scheme

The two-photon excitation starting at the hyperfine ground state $5S_{1/2}$ F = 3 can be seen in Fig. 5.1. The main purpose of the pump laser is the transfer of population from the ground state to the intermediate state $5P_{3/2}$ $F' = 4$. Once excited to the 5P state, further transfer to the 4D states is possible at a wavelength of 1529 nm. The 4D state's fine and hyperfine structure are inverted, which means the $4D_{5/2}$ state lies below the $4D_{3/2}$ state energetically. For the same reason, the $F'' = 5$ hyperfine state is the lowest. This anomaly is popular in many other nD and nF states of alkali metals [24]. The main reason is the second order perturbation of the interaction between core and valence electrons. For the case of nD and nF states this correction term is negative which leads to the inverted structure [25–27].

Typically, Doppler-free spectroscopy of hot atomic vapors is possible with at least two lasers. Saturation spectroscopy [28] uses two laser beams passing through the vapor. By that the pump laser selects atoms with a certain velocity resonant with the laser frequency. Meanwhile, the probe laser illuminating the same volume experiences transmission through the same atoms. Thus, the monitored probe signal shows no Doppler broadened spectrum for a hot atomic gas. This velocity selection is not limited to one laser transition or to the same wavelength [29].

For the counter-propagating case depicted in Fig. 5.1 the velocity selection is given by the 780 nm pump beam. Since each hyperfine level is Doppler broadened, the levels overlap. The locked pump laser is resonant with different velocity classes for

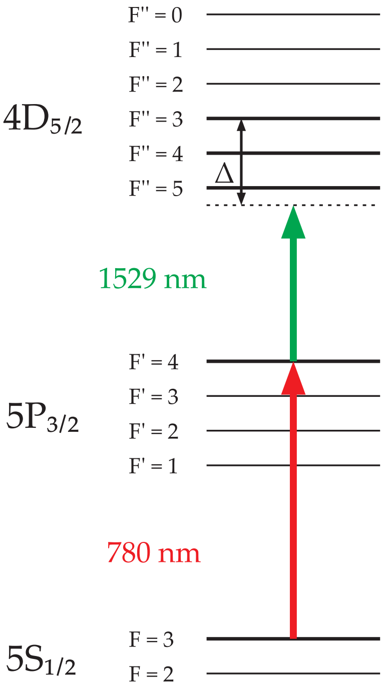

Figure 5.1.: Two-photon excitation scheme for ^{85}Rb. The 780 nm pump laser is locked to the $5S_{1/2}$ $F = 3 \to 5P_{3/2}$ $F' = 4$ transition while the 1529 nm probe laser is scanned over the $4D_{5/2}$ states (black arrow).

each Doppler broadened and dipole allowed hyperfine level of the 5P state. The atoms excited to the 5P state are further excited to the 4D state by the scanning probe laser. Due to the difference in wavevector, the frequency spacing between the 5P hyperfine levels is different from the values provided in the appendix. The influence of the residual Doppler effect on the spectrum will be discussed in the following.

5.2. ^{85}Rb 4D$_{5/2}$ Spectrum

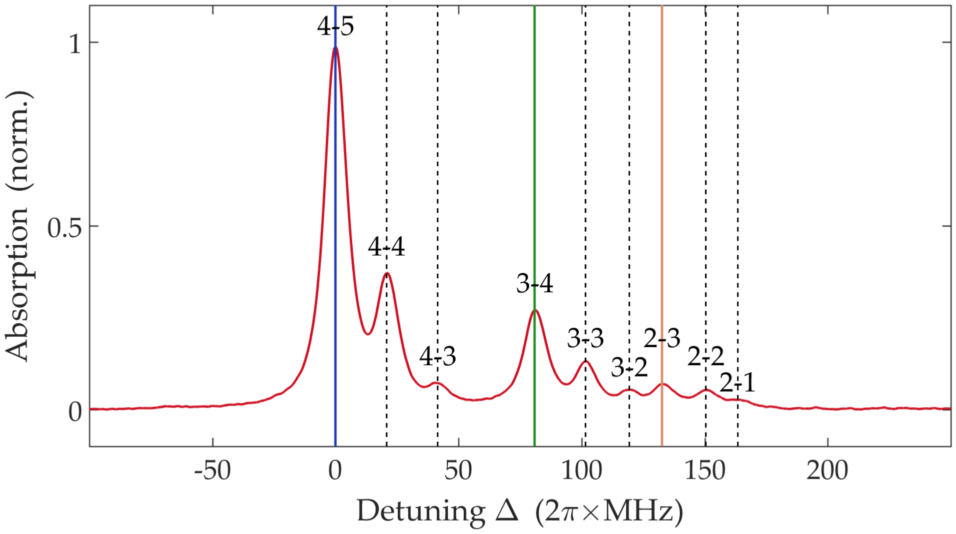

FIGURE 5.2.: ^{85}Rb counter-propagating two-photon absorption spectrum in the reference cell. The numbers above the peaks refer to the hyperfine transitions from 5P$_{3/2}$ F′ to 4D$_{5/2}$ F″. Theoretical peak positions are marked with vertical lines. Solid lines mark the first transition of three individual sub-features.

The ^{85}Rb isotope shows nine distinct peaks in the 4D spectrum as depicted in Fig. 5.2. Each hyperfine transition from 5P to 4D is identified, e.g. the transition from 5P$_{3/2}$ $F' = 4$ to 4D$_{5/2}$ $F'' = 3$ is labeled as '4-3'. The black vertical line spacing corresponds to the level spacing in the appendix 'Properties of Rubidium'. However, the green and yellow vertical lines are calculated as follows for the case of counter-propagating beams. The resonant transition from 5S$_{1/2}$ F= 3 to 5P$_{3/2}$ $F' = 4$ and the second transition to 4D$_{5/2}$ $F'' = 5$ for atoms with $v = 0$ along the laser axis is depicted on the left side of Fig. 5.3. The resonance frequency of the probe laser is given by ω_1 for that case.

Atoms moving away from the pump laser with the 'right' velocity can be excited from 5S$_{1/2}$ F= 3 to the lower lying hyperfine level 5P$_{3/2}$ $F' = 3, 2$. The probe laser is then resonant at ω_2 as shown in Fig. 5.3. Also, the atoms excited to the 5P$_{3/2}$ $F' = 3$ state can only do a transition to the dipole allowed ($\Delta F = \pm 1, 0$) states 4D$_{5/2}$ $F'' = 4, 3, 2$. Then, the scan of the probe laser allows to hit a resonant transition ω_2 to the 4D states.

In order to calculate the spacing between the blue and green vertical line in

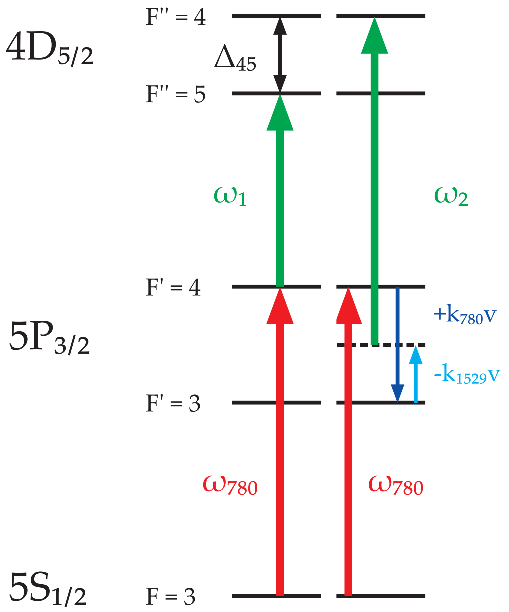

Figure 5.3.: Origin of the sub-feature of the counter-propagating two-photon spectrum of ^{85}Rb. Due to the Doppler effect excitation of off-resonant 5P hyperfine levels is possible. The resonant transition for zero velocity is depicted on the left with ω_1 and the resonant transition due to the Doppler effect is shown on right with ω_2.

Fig. 5.2, one has to calculate the difference between the two excitation paths:

$$\begin{aligned}\delta_{\mathrm{res}}^{34} &= \omega_2 - \omega_1 = \Delta_{45} + v(k_{780} - k_{1529}) \\ &= \Delta_{45} + k_{780} v \left(1 - \frac{k_{1529}}{k_{780}}\right) \\ &= 20.75\ \mathrm{MHz} + 120.64\ \mathrm{MHz} \cdot (1 - 0.5102) = 79.84\ \mathrm{MHz}.\end{aligned} \tag{5.1}$$

The velocity v refers to atoms resonant with the $5S_{1/2}$ F$=3 \rightarrow 5P_{3/2}$ F$'=3$ transition. The same calculation for the green and yellow line in Fig. 5.2 yields a spacing of $\delta_{\mathrm{res}}^{23} = 51.50$ MHz. In total, three sub features with three hyperfine transition are visible due to the Doppler effect. Theoretically, even the transition from $5P_{3/2}$ F$'=1$ to $4D_{5/2}$ F$''=2,1,0$ could be observed in Fig. 5.2. However, due to the dipole-forbidden transition from $5S_{1/2}$ F$=3$ to $5P_{3/2}$ F$'=1$ this level can only be populated through spontaneous emission from higher 4D levels leading to a much smaller population in that state (for weak probe). Also, calculations show that the $5P_{3/2}$ F$'=2 \rightarrow 4D_{5/2}$ F$''=1$ overlaps with the theoretical $5P_{3/2}$ F$'=1 \rightarrow 4D_{5/2}$ F$''=2$ transition which has the largest amplitude of that sub feature. Note that due to nonlinear frequency scaling of the scan ramp which cannot be fully

compensated using an FPI with a FSR of ≈ 2 GHz, the vertical lines are adjusted relative to the main transition 4-5 by 1 MHz in Fig. 5.2.
A fit function for further understanding of the spectrum and comparison to the evanescent signal is desirable. The derivation of the fit function will be discussed and applied to the spectrum in the following section.

5.2.1. Two Photon Fit Function

A detailed discussion of the fit function of the D$_2$-line of rubidium can be found in [30]. Here, some of the main aspects will be discussed and compared to the measured data.
For the excitation scheme in this experiment one can assume a two level system where the lower state is defined as 5P and the upper state as 4D because the lower pump laser only transfers population from the actual ground state 5S. However, the population of the 5P states can not simply be approximated as a thermal equilibrium distribution but depends on the dipole matrix elements of the hyperfine transitions from 5S to 5P. The fit function can be separated into a product of amplitude and line shape.
Since all performed measurements were done with arbitrary signal scale (y-axis), it makes sense to define an overall amplitude prefactor A_0. However, the relative amplitudes of the individual peaks are given by the dipole matrix transition element which one has to calculate for each individual transition from 5S to 5P and from 5P to 4D. So, one has to calculate

$$\langle F, m_F | e\mathbf{r} | F', m'_F \rangle \tag{5.2}$$

with m_F being the Zeeman hyperfine sub-levels. Explicitly, one has to calculate the contribution of the wave functions applied to the dipole operator $\mathbf{d}$. Nevertheless, the Wigner-Eckart theorem [31] allows for a simplified notation and calculation of the dipole operator for a given set of angular momenta $\{F, F'\}$. The idea is to reduce the expression in Eq. 5.2 to the simplest form, since the total angular momentum $\mathbf{F}$ consists of a sum of spin angular momentum $\mathbf{S}$, nuclear angular momentum $\mathbf{I}$ and orbital angular momentum $\mathbf{L}$. The theorem predicts a linear dependence of the full expression in Eq. 5.2 to its reduced forms. Therefore one can write [32]

$$\langle F, m_\mathrm{F} | e\mathbf{r} | F', m'_\mathrm{F} \rangle = \langle F || e\mathbf{r} || F' \rangle \, (-1)^{F'-1+m_F} \sqrt{2F+1} \begin{pmatrix} F' & 1 & F \\ m'_F & q & -m_F \end{pmatrix} \tag{5.3}$$

with the contribution of the hyperfine sub levels given by the Wigner 3-j symbol and the component of $\mathbf{r}$ interacting with the light, which is basically a polarization dependent property ($q = 0$ for linearly polarized light and $q = \pm 1$ for circular polarization). The Wigner 3-j symbol is a further simplified version of the more general Clebsch-Gordon coefficient [33]. This simplification can be done due to the symmetry of the system. Again, the expectation value in Eq. 5.3 for the dipole operator can be reduced to

$$\langle F || e\mathbf{r} || F' \rangle = \langle J || e\mathbf{r} || J' \rangle \, (-1)^{F'+J+1+I} \sqrt{(2F'+1)(2J+1)} \begin{Bmatrix} J & J' & 1 \\ F' & F & I \end{Bmatrix} . \tag{5.4}$$

Here, the Wigner 6-j symbol is a product of four Wigner 3-j symbols. The reduced dipole moment $\langle J || e\mathbf{r} || J' \rangle$ is provided in the appendix. Assuming linear polarization only, the Wigner 3-j symbol in Eq. 5.3 yields $\frac{1}{3}$. Finally, the total relative amplitude for a single two-photon hyperfine transition A_i is given by

$$A_i = | \langle F, m_F | \, e\mathbf{r} \, | F', m'_F \rangle |^2 \cdot | \langle F', m'_F | \, e\mathbf{r} \, | F'', m''_F \rangle |^2 , \tag{5.5}$$

with $i = 1 \ldots 9$ representing the nine observed hyperfine peaks while F,F$'$ and F$''$ refer to the fine structure 5S, 5P and 4D, respectively.

In the 'Atom Light Interaction' chapter it was shown that for a thermal vapor the line shape of the imaginary part of the susceptibility follows a Voigt profile in the most general form. As mentioned in the theory chapter, there is no analytic expression for the Voigt profile and a numerical fit approach is time consuming. In order to enable Voigt fitting on a reasonable time scale approximations have to be made. The Voigt profile in this experiment follows the idea of an approximated analytic expression of the Voigt profile with the Gaussian standard deviation σ and the Lorentzian FWHM 2γ being the only fit parameters. An approach [34] for the Voigt profile is given by

$$V(X,Y) = \sum_{i=1}^{4} \frac{C_i(Y - A_i) + D_i(X - B_i)}{(Y - A_i)^2 + (X - B_i)^2} , \tag{5.6}$$

where $X = \frac{\Delta}{\sigma\sqrt{2}}$ and $Y = \frac{\gamma}{\sigma 2\sqrt{2}}$ provide the contribution from Lorentzian and Gaussian line shapes. The coefficients A, B, C, and D can also be taken from [34]. The previous section has shown that the probe laser is interacting with atoms of three different velocity classes which is caused by the Doppler effect. This means that the three sub features j have to be weighted with the Boltzmann distribution for the corresponding velocity $A^j_{\mathrm{MB}}(v_j)$.

Thus, the total expression for the imaginary part of the susceptibility for a single hyperfine transition is given by $\alpha_{i,j} = A_0 A^j_{\mathrm{MB}} A_i V_i(\Delta, \Delta^i_0, \sigma, \gamma)$. Typically, one has to define a reference position Δ_0 for the spectrum. For that purpose, the largest transition from $5P_{3/2}$ F$'$ = 4 to $4D_{5/2}$ F$''$ = 5 (cyclic transition) was chosen as

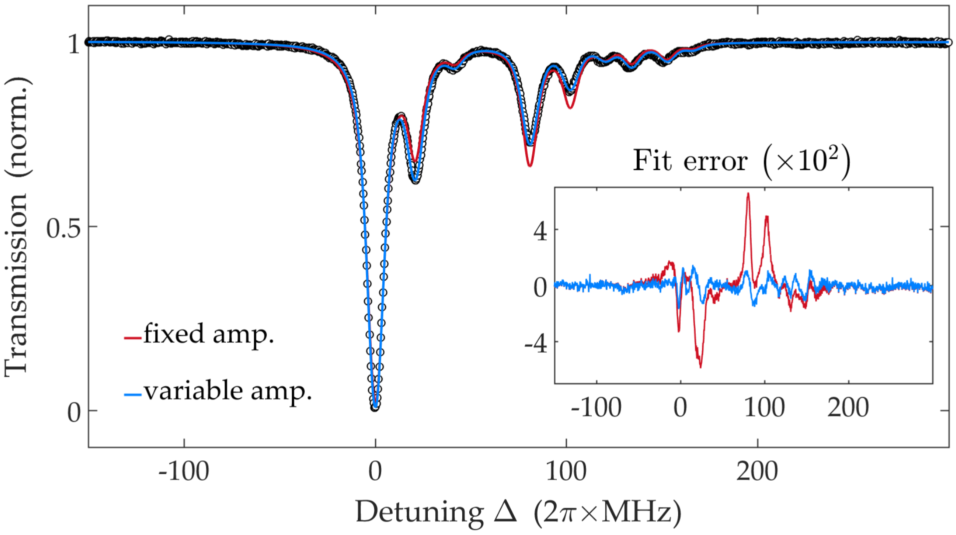

FIGURE 5.4.: Voigt fit of the 4D spectrum of ^{85}Rb in the reference cell with counter-propagating beams with fixed (red) and variable (blue) relative amplitudes. Inset: Fit error for the same detuning and matching color code. The probe power is 20 μW and the pump power is 100 μW.

reference peak at zero detuning. This allows one to take the level spacings in the appendix and directly insert them for Δ_0^i to obtain every hyperfine peak relative to the main transition. In the 'Atom Light Interaction' chapter the spectrum is finally given by the transfer function T. Hence, the final fit function is given by

$$f(\Delta) = \sum_{j=1}^{3} \sum_{i=3j-2}^{3j} \exp(-\alpha_{i,j}(\Delta' \cdot (\text{lsx} + \Delta'\text{nlsx}))l_0) \cdot L + S\Delta + O_1\Delta + O_0. \quad (5.7)$$

Here, fit parameters were added to compensate for experimental errors: First of all, the peak position of the main transition Δ_0 has to be found and the absorption coefficient α has to be scaled accordingly with $\Delta' = \Delta - \Delta_0$. Additionally, depending on the scan ramp, the signal might be the mirror image of the expected spectrum. Also nonlinear scaling of the frequency axis especially for larger detuning ($\approx$ 10 GHz) can be compensated with a second order polynomial. The parameters lsx $= \pm 1$ and nlsx account for those effects. The length of the cell is included via l_0. The amplitude of the light level L, the slope of the signal S and a linear (O_1) and constant (O_0) offset compensate for the remaining experimentally caused effects.
The fit procedure works as follows: First, a polynomial fit to the slope of the signal is made and subtracted from the data. Then, the fit function from above is applied. However, instead of using a Voigt, a Gaussian line shape is used at

first. This gives rough values for all fit parameters. Afterwards, those fit parameters are used as starting guesses for the final Voigt fit. The result of the fit is shown in Fig. 5.4 with the red curve. Some deviations from the measured data are observable, especially for the second sub feature ($5P_{3/2}$ $F' = 3 \rightarrow 4D$). This discrepancy originates from two additional effects: Pumping effects into different undesired states caused by decay from upper transitions and not purely linearly polarized light. The calculation assumes perfect linear polarization, and a weak probe. Those effects cause deviations from the calculated peak amplitudes. The main focus lies on the position of the peaks, for that reason eight additional fit parameters were used to overcome the deviation from the measurement. They were used as relative prefactors $1 - p_i$ for all eight peaks excluding the main transition allowing variables relative amplitudes. The result of that approach can be seen in Fig. 5.4 with the blue curve. The inset presents the fit quality for both cases. For a better fit, all following data hyperfine fits are performed with variable amplitudes. Note that the expression for the fit function was derived for a two level atom in the 'Atom Light Interaction' chapter. The following sections discuss the influence of probe power, pump power and temperature on the spectrum.

5.2.2. Saturation

Fig. 5.5 shows the 4D spectrum for probe powers P_{1529} from 10μW to 4.5 mW in logarithmic steps. After reaching probe powers of 2 mW the linewidth visibly increases and the amplitude decreases. The fit follows the measured data until it starts to saturate significantly. Each hyperfine transition exhibits a slightly different linewidth which is proportional to the dipole matrix transition element of the corresponding transition and, hence the Rabi frequency. By increasing the intensity, each hyperfine linewidth is multiplied by the same factor $\sqrt{1 + I/I_{\text{sat}}}$. This causes the difference in linewidth to increase as well. The fit assumes the same linewidth for every hyperfine transition and thus shows a worse overlap with the measured data for higher power.
The intensity can be calculated from the power as

$$I = \frac{P}{A} = \frac{P}{\pi w^2}. \tag{5.8}$$

The illuminated area A is approximated for the Gaussian mode with w being the waist of the beam.

One method to measure the beam waist is the knife-edge measurement [35]. By gradually moving in a knife edge into the beam profile and simultaneously monitoring the power, the power-knife position diagram follows an error function which

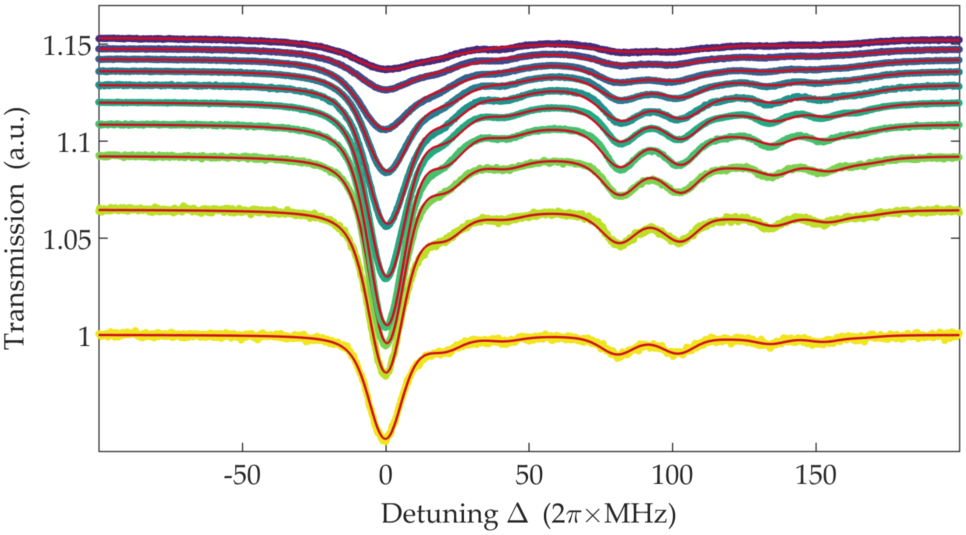

FIGURE 5.5.: 4D spectrum of ^{85}Rb with counter-propagating beams in the reference cell with increasing probe power $P_{1529} = 0.01 \ldots 4.5$ mW from bottom to top. Red curves show the fits. The pump power was fixed at 0.5 mW.

can be fitted to extract the waist. In this experiment, the waist of the reference probe beam is $w \approx 1.5$ mm, and the ellipticity is 1. The fitted Voigt FWHM is plotted over the logarithmic intensity with the measured waist in Fig. 5.6. This width was calculated from the fitted Gaussian $\Delta\omega_{\mathrm{G}}$ and Lorentzian $\Delta\omega_{\mathrm{L}}$ width using the empirical formula [36]

$$\Delta\omega_{\mathrm{V}} \approx 0.5346\Delta\omega_{\mathrm{L}} + \sqrt{0.2166\Delta\omega_{\mathrm{L}}^2 + \Delta\omega_{\mathrm{G}}^2}. \tag{5.9}$$

The fit function 5.10 follows the theory but adds an additional broadening Γ_+ due to other broadening effects: Since the wavevector difference between the two lasers is noticeable, the atoms excited to the 4D states are not fully at rest but have a finite velocity. This causes inhomogeneous residual Doppler broadening. One way to overcome this issue is to double pass the reference cell with the probe beam. The other effect, the splitting of the lines, comes from the actual three level character of the system. Note that the effect appears with two levels alone, but the probe excitation to the third level is what makes it visible. The basic concept is the splitting of the intermediate state 5P into two levels due to strong pump lasers or AC fields in general. This is the so called AC Stark effect or Autler-Townes effect [37], which will be discussed in the next section. If the splitting is actually smaller than the linewidth of each individual peak, the window between the two split peaks is buried in between and only manifest itself in an increase of the

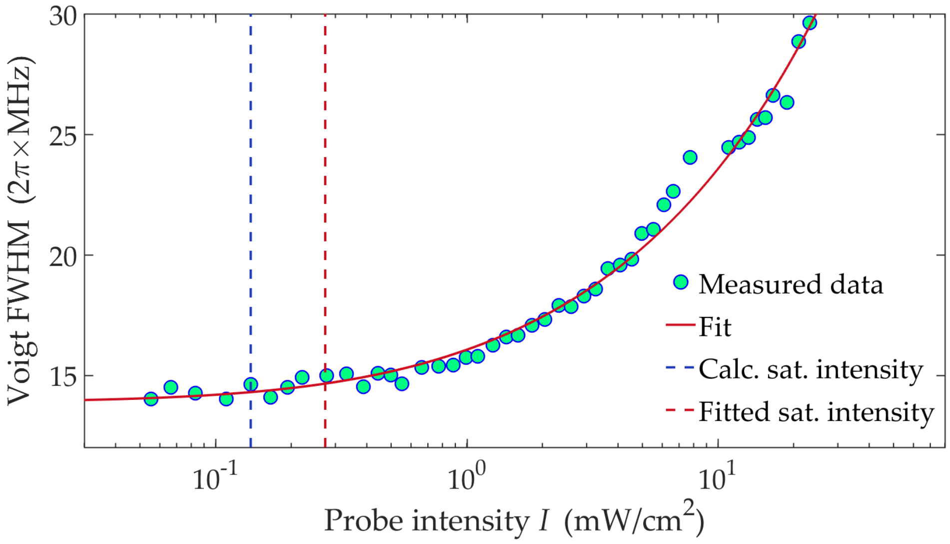

Figure 5.6.: FWHM from the Voigt fit as a function of intensity. The fit shows a square root behavior. Calculated and fitted saturation intensity is marked with dashed lines.

linewidth. For fairly low pump powers, here $\Omega_{780}/\Gamma \approx 1/3$, this effect should not appear. In order to compensate for the residual Doppler as well as for uncertainties in the pump and probe power, the fit function reads

$$f(I) = \Gamma\sqrt{1 + \frac{I}{I_{\text{sat}}}} + \Gamma_{+}. \tag{5.10}$$

With $\Gamma = 1/\tau$ in $2\pi\times$MHz and I_{sat} and Γ_{+} as only free fit parameters one obtains a measured saturation intensity of 0.27 ± 0.02 mW/cm^2. The calculated saturation intensity 0.138 mW/cm^2 (blue) is marked together with the measured saturation intensity (red) in Fig. 5.6. The measured value is roughly twice as large as the calculated one. Still, it is a reasonable value considering the uncertainty of the beam waist and the probe power.

5.2.3. Autler-Townes Effect

In their works [37], Autler and Townes found that the frequency spacing between the split peaks has the same frequency as the applied (rf-) field. This fact allows precise determination of the Rabi frequency of the pump laser in this experiment. Thus, by gradually increasing the pump power all hyperfine peaks continuously split into two peaks as shown in Fig. 5.7. As a result, hyperfine peaks close to each other start to disappear since the overlapping states now have to share their population with

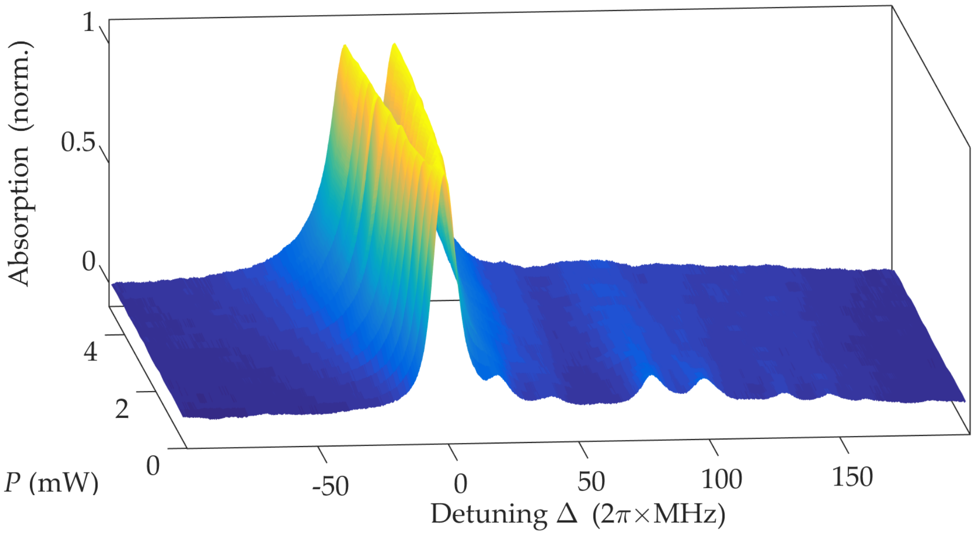

FIGURE 5.7.: Autler-Townes splitting of the ^{85}Rb 4D spectrum, plotted for different pump powers from 0.25 mW (front) to 4.85 mW (back) over the probe detuning Δ. The probe power was fixed at 5 μW.

each other. The overall amplitudes of those peaks decrease and they smear out, as one can see for the transitions from $5P_{3/2}$ $F' = 3, 2$ to 4D. The simplest theoretical foundation of this phenomenon is given by the Jaynes-Cummings model [38], where the split states are the result of strong atom light coupling.

The splitting corresponds directly to the Rabi frequency of the pump laser. Thus, the measured splitting can be compared to the calculation for the Rabi frequency. The comparison of the expected (calculated) Rabi frequencies and the actual values is depicted in Fig. 5.8. The blue curve was obtained by measuring the pump power with a power meter and then calculating the corresponding Rabi frequencies via

$$\Omega = \frac{|d_{\text{eff}}||E|}{\hbar} = \frac{|d_{\text{eff}}|}{\hbar}\sqrt{\frac{4P}{\pi w^2 c \epsilon_0}}, \tag{5.11}$$

with the effective dipole moment $d_{\text{eff}} = 2.06937 \cdot 10^{-29}$ Cm [39] and maximum intensity $I_{\max} = 2P/(\pi w^2)$. The waist w of the pump beam is 1.7 mm.

Clearly, the calculated data does not fit to the observed peak splitting. The main sources of the deviation are probably the measured power and actual pump beam waist in the vapor cell. Also, the Rabi frequency decreases while the laser propagates through the 10 cm vapor cell, so it cannot be approximated with the given formula solely. However, this measurement allows for a calibration of the Rabi frequency (or power). The split main transition is fitted with a Lorentzian each. The difference

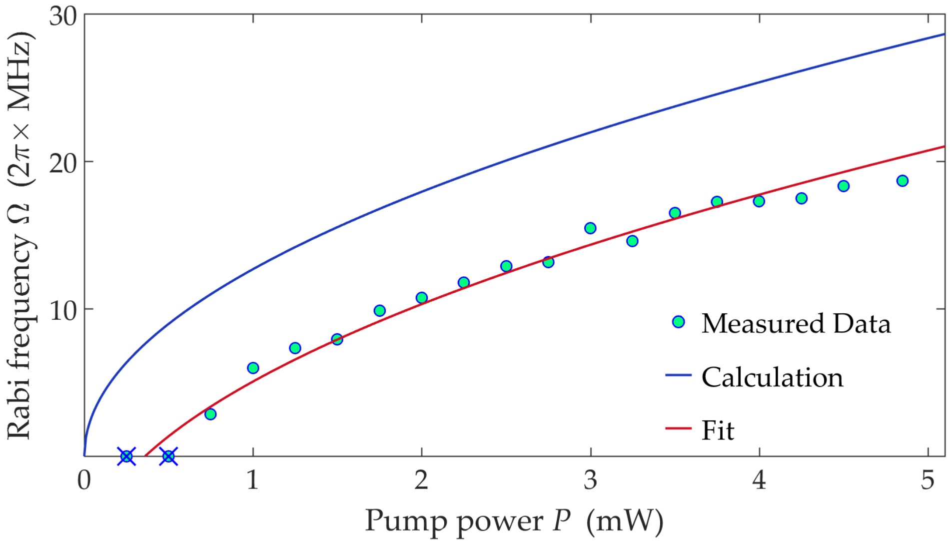

Figure 5.8.: Measured pump Rabi frequency in relation to its power (circles). The red line is a fit to the measured data and the blue line shows the simulation for the same pump power.

in their fitted peak position corresponds to the measured data depicted in Fig. 5.8. This still results in small fit errors on the order of ≈ 1 MHz. Other errors occur from fluctuating pump power during the measurement. In total, those errors are much smaller than the errors in measured power and expected waist. In order to obtain more precise Rabi frequencies for arbitrary pump powers before or after splitting, a fit function was used that expects a loss in Rabi frequency R_0 with one free fit parameter

$$f(P) = \frac{|d_{\mathrm{eff}}|}{\hbar}\sqrt{\frac{4P}{\pi w^2 c\epsilon_0}} - R_0. \tag{5.12}$$

The fit shown in Fig. 5.8 yields $R_0 = 7.622 \pm 0.381$ MHz. Further calculations of the Rabi frequency will be adjusted with this parameter obtained from this fit.

5.2.4. Co- vs. Counter-Propagating Excitation

So far only the counter-propagating scheme was considered. For further discussion of the measured data, a study of the co-propagating spectrum is useful, as well. Fig. 5.9 shows why the counter-propagating excitation is favorable: Since in the co-propagating case both wavevectors point in the same direction, atoms with a wider range of velocities can be excited. This leads to a broadened two-photon spectrum where the hyperfine peaks can hardly be resolved. A more detailed

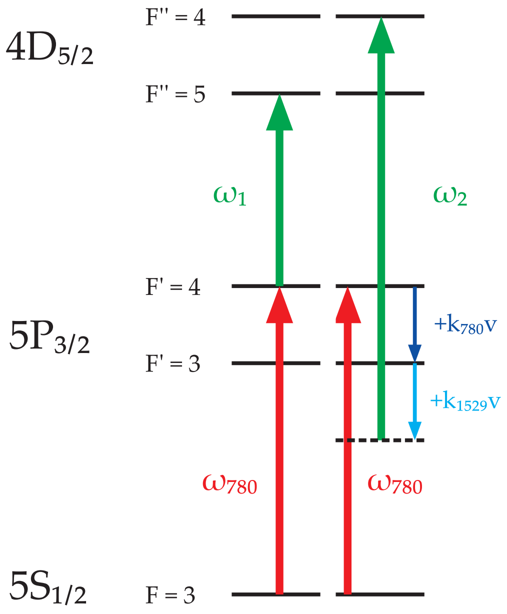

FIGURE 5.9.: Co-propagating excitation of ^{85}Rb. The left part shows both lasers on main resonance while the right side depicts the excitation of the second sub feature due to the Doppler effect.

study of the difference between co- and counter-propagating rubidium spectrum can be found in [40, 41], where one expects three sub features as it is the case for counter-propagating beams. The spacing between those sub features can be calculated from the different excitation paths in Fig. 5.9.

$$\begin{aligned}\delta_{\text{co}}^{34} &= \omega_2 - \omega_1 = \Delta_{45} + v(k_{780} + k_{1529}) \\ &= \Delta_{45} + k_{780}v\left(1 + \frac{k_{1529}}{k_{780}}\right) \\ &= 20.75\text{ MHz} + 120.64\text{ MHz}\cdot(1+0.5102) = 202.94\text{ MHz}.\end{aligned} \tag{5.13}$$

The third sub feature can be found $\delta_{\text{co}}^{23} = 116.50$ MHz away from the second one. The fit for this spectrum follows the description of the counter-propagating case, but the locations of the sub features are adjusted accordingly. The results are shown in Fig. 5.10 for variable amplitudes. The individual hyperfine peaks are barely visible. The spacing between the blue and green vertical line is δ_{co}^{34} while the spacing between green and yellow line is δ_{co}^{23}. The whole spectrum shows larger spacings between the sub features than the counter-propagating counterpart due to the larger residual Doppler effect with parallel wavevectors.

An unwanted effect that arises from the reflectivity of the reference cell's mirrors

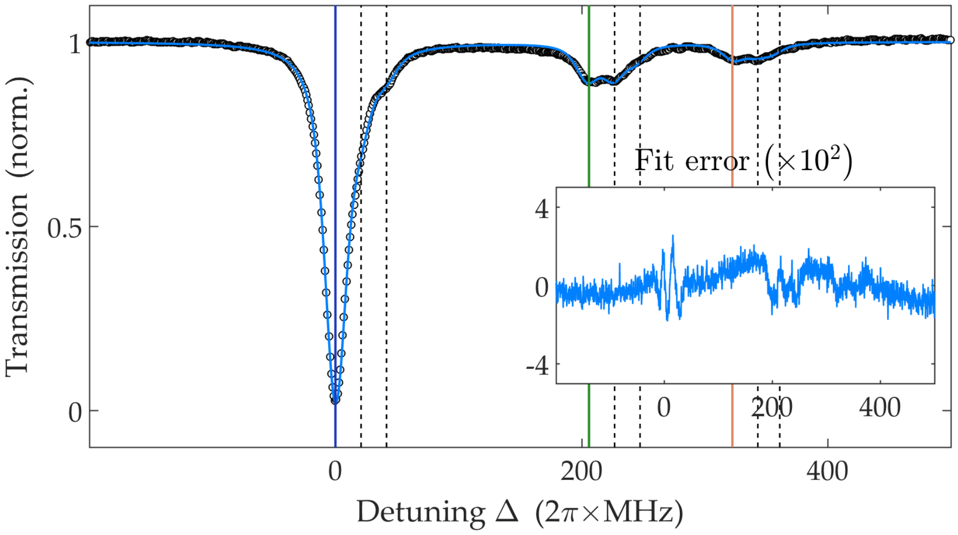

Figure 5.10.: Co-propagating ^{85}Rb spectrum in the reference cell with corresponding fit function. Vertical lines mark the calculated sub features' main peak position following the notation in Fig. 5.2. Inset: Fit error over the same detuning range. The probe power was fixed at 150 μW and the pump power is 100 μW.

is the observation of co- and counter-propagation at the same time. This is due to some parts of the pump (and probe) beam being reflected at the opposite window. The reflected pump overlaps slightly with the probe beam in a co-propagating configuration or vice versa for the co-propagating scheme. One can increase this effect in two ways: 1) By increasing the density, the absorption signal is much stronger and therefore, the contribution of the weak reflection is more visible. 2) By increasing the pump power far beyond splitting to enhances the visibility of the other configuration. The latter is done in Fig. 5.11. The temperature in the reference cell was determined to be 38°C by scanning the 780 nm pump laser and fitting the D_2 line with the same procedure as described for the two photon case. For pump powers around 2 mW a noticeable peak appears at ≈ -200 MHz. This peak is identified as the main peak of the co-propagating spectrum. The shift of 204 MHz between the two main transitions originates from the frequency shift of the AOM: The internal radio frequency of the AOM is 200 MHz. The 780 nm pump laser locked to the $5S_{1/2}$ F= 3→$5P_{3/2}$ F′ = 4 transition is detuned by that internal radio frequency. So, the atoms addressed by the pump laser have a velocity $v_{\mathrm{AOM}} = \frac{\Delta_{\mathrm{AOM}}}{k_{780}}$. In the frame of the probe laser, the Doppler effect leads to an effective detuning of

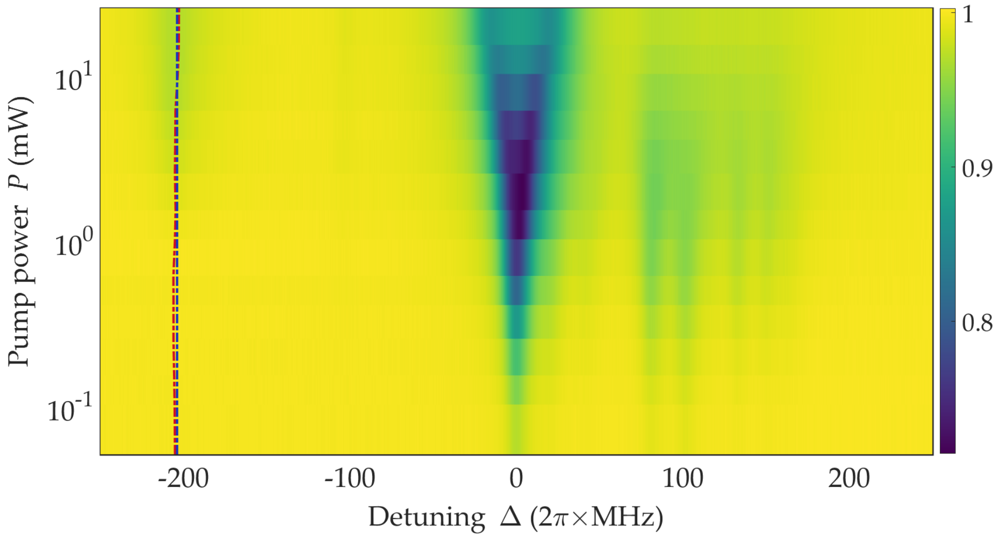

FIGURE 5.11.: Counter-propagating ^{85}Rb transmission spectrum in the reference cell at $T = 38°$ C for increasing pump power. The color bar shows the normalized transmission. The peak at around -200 MHz belongs to the co-propagating spectrum. Vertical lines mark the fitted (red) and calculated position (blue) of the cyclic transition of the co-propagating configuration.

$$\Delta_{\mathrm{AOM}}^{\mathrm{eff}} = \pm v_{\mathrm{AOM}} k_{1529} = \pm \frac{\Delta_{\mathrm{AOM}}}{k_{780}} k_{1529} = \pm 102.0\ \mathrm{MHz}. \tag{5.14}$$

The positive/negative prefactor corresponds to counter- and co-propagating configuration, respectively. The total shift between counter- and co-propagating main transition yields 204 MHz and is drawn as blue dashed line in Fig. 5.11. The red dashed line corresponds to the fitted position of the peak with an average value of 204.5 MHz, which is in perfect agreement with the expected position.

Coincidentally, the largest peak of the second sub feature in the co-propagating spectrum with a spacing of 203 MHz towards the blue (positive detuning) overlaps with the main peak of the counter-propagating spectrum. By increasing the pump power towards splitting this second sub feature leads to a decrease of the transparency window between the two split main peaks of the counter-propagating spectrum. The same observation can be made for the co-propagating spectrum. Note that by choosing the '-1' instead of the '+1' diffraction order of the AOM, it is possible to shift the spectrum of the other configuration by +204 MHz avoiding the overlap of the two spectra.

5.3. Comparison with ^{87}Rb

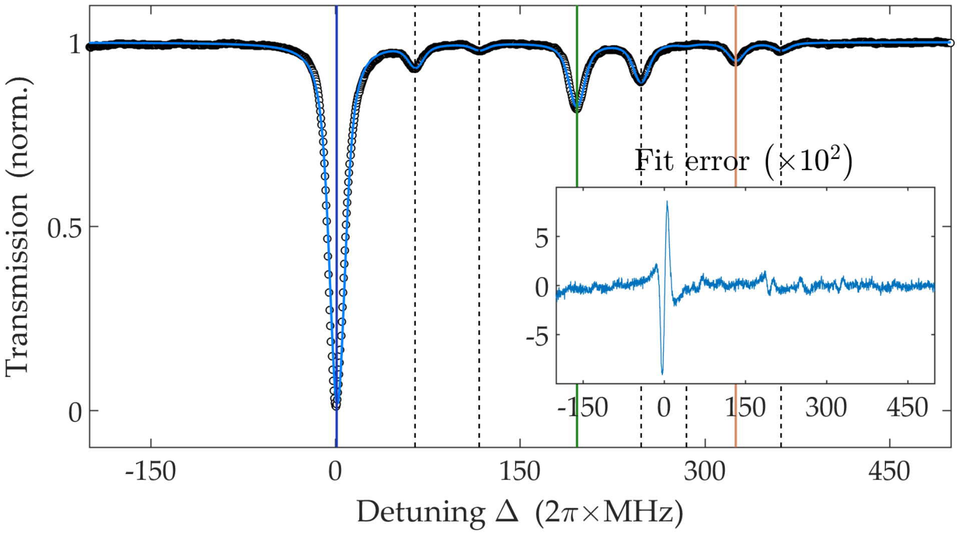

Figure 5.12.: ^{87}Rb 4D spectrum for counter-propagating beams in the reference cell with corresponding fit. The vertical lines mark the calculated peak position following the notation from previous plots. Inset: Fit precision of the same detuning range. The probe power was set to 150 μW and the pump power was 400 μW.

The characterization of the two photon reference setup was mainly done with the ^{85}Rb isotope. However, for sake of completeness a brief analysis of the ^{87}Rb isotope will be presented in this section.

The main difference between the isotopes is the nuclear spin I. ^{87}Rb has a nuclear spin of 3/2 whereas ^{85}Rb has a nucear spin of 5/2. This influences the level scheme as one can see in Fig. 5.13. The $4D_{5/2}$ states only contains four peaks with F = |J-I|,...|J+I| = 1,2,3,4. Thus, there are only two hyperfine transitions from the Doppler detuned state $5P_{3/2}$ $F' = 1$ to the 4D states, reducing the total number of peaks from nine to eight. Since the hyperfine spacing of the 5P and 4D states for ^{87}Rb is much larger than the spacing of ^{85}Rb, the residual Doppler shift is also larger. Hence, the full ^{87}Rb spectrum spans roughly 400 MHz.

The spacing between the first (blue) and second (green) sub feature yields 194.3 MHz. The distance from the green to the yellow line in Fig. 5.12 is 129.0 MHz. The fit shows good agreement with the measured data.

The fit function is very similar to the version for ^{85}Rb, except the missing ninth peak and new spacings. The quality of the fit is depicted in Fig. 5.12 (inset). It seems that the position of the fitted main peak is slightly shifted for that particular

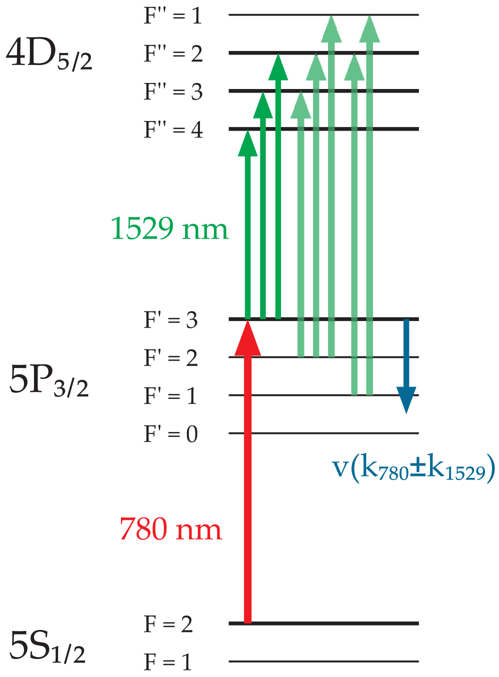

Figure 5.13.: Level scheme for the ^{87}Rb excitation with all transitions corresponding to the peaks in Fig. 5.12. The residual Doppler detuning is shown with a blue arrow.

measurement, which is why the fit error is comparably large around zero detuning. This could be caused by a not completely linear scan ramp. Also, due to the very small transition dipole matrix element, the transition from $5P_{3/2}$ $F' = 2$ to $4D_{5/2}$ $F'' = 1$ is barely visible in the spectrum. The calculated position is marked with a dashed vertical line at ≈ 280 MHz.

6. Evanescent Spectrum

This chapter presents the novel measurements of evanescent excitation of the rubidium 4D state at a silicon surface in a thermal atomic vapor.
The transition from a dispersive to an absorptive signal at the critical angle is demonstrated with the wafer cell. Density dependent measurements were performed to find the optimum operation temperature. An observed shift of the wafer spectrum relative to the reference spectrum is studied in detail. The regime of the power broadening is determined and the effect of the polarization on the evanescent field power is explained. Different penetration depths were achieved by changing the angle of incidence and their influence on the reflection spectra is studied.

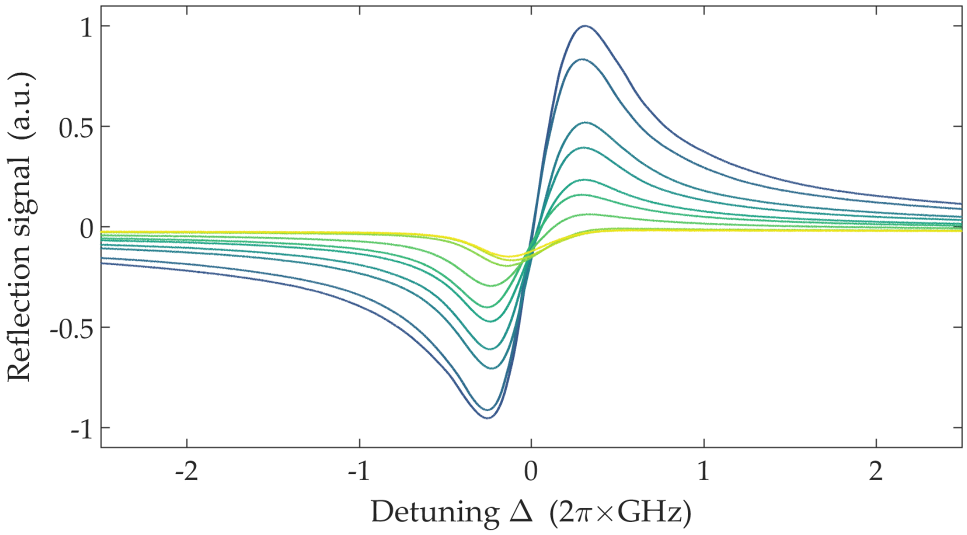

FIGURE 6.1.: Measured transition from a dispersive to an absorptive signal at the critical angle θ_C for ^{85}Rb at the interface Si→vapor. The angle of incidence continuously changes from below the critical angle (blue) to larger angles above the critical angle (yellow).

The section finally combines all introduced effects and observations of the Doppler-free spectrum. All measurements in this chapter were carried out in the oven (see 'Setup' chapter) with the beam configuration that is shown in the right picture of Fig. 4.7.

In order to induce interaction between atoms excited to the 5P state with the evanescent probe field, the 1529 nm telecom laser is coupled into the ZnSe prism as depicted in the 'Setup' chapter. By monitoring the reflected signal 'R' (see Fig. 4.8), one can study the effects of the evanescent field on the spectrum.

The reflected signal's lineshape can change depending on the angle of incidence θ_{Si} (compare with Fig. 4.8). This measured effect is depicted in Fig. 6.1. Before discussing the origin of this behavior, some main differences to the previously studied hyperfine spectrum will be explained.

First of all, there is no visible hyperfine structure due to the configuration of the lasers. In all cases the pump wavevector (corresponding to the direction of propagation) is perpendicular to the probe. Hence, all atoms with velocity classes addressed by the pump will further be excited by the probe beam leading to a fully Doppler broadened spectrum. In contrast to the hyperfine signal, the detuning scale reads GHz. Additional broadening is caused by higher temperatures (50°C to 130°C), a larger wavevector, and transit time effects.

The second difference is noticeable in the signal to noise ratio of the data. For all following measurements a Lock-In amplifier (Stanford Research Systems Model SR830 DSP) was used. Due to larger reflections of the probe beam propagating through various boundaries with dramatic changes in refractive index one has to filter out the contributions of the reflection from the actual atomic signal. Also, the probed volume is small compared to the reference cell leading to generally small signals. The amplitude modulation frequency of the pump is always kept at 100 kHz. The photo diode has a bandwidth of

$$\Delta f = \frac{1}{2\pi R_{\text{load}} C} = 796\,\text{kHz} \tag{6.1}$$

with a load of $R_{\text{load}} = 50\ \Omega$ and a junction capacitance $C = 4$ nF. The integration time is 0.1 ms.

The case of transition from a dispersive to an absorptive feature by changing the angle of incidence is depicted in Fig. 6.1. The 'Evanescent field' together with the 'Atom Light Interaction' chapter gives a simple explanation for that behavior. From the latter, one knows that the refractive index of the vapor is given by $n_2 = \sqrt{1+\chi}$. Inserting this into the expression for the derived reflection coefficient and using a Taylor approximation to first order in susceptibility [42] yields

$$r = r_0 \left(1 - \frac{n_1 \cos(\theta_{\text{in}})\chi}{(n_1^2 - 1)\beta}\right) \tag{6.2}$$

with zero order approximation r_0 and $\beta = \sqrt{1 - n_{\text{Si}}^2 \sin(\theta_{\text{in}})^2}$. Eq. 6.2 is plotted for different angles below the critical angle of 16.6° in Fig. 6.2. The width appears

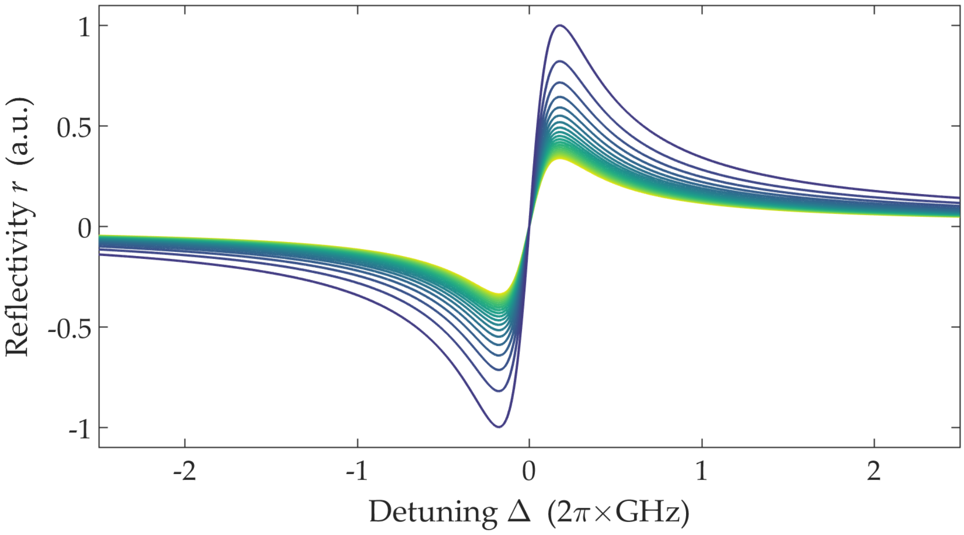

FIGURE 6.2.: Reflectivity for angles of incidence from 10° to 16° in steps of 0.3° at the interface Si→vapor. The amplitude increases getting closer to the critical angle of 16.6° from yellow to blue.

smaller than in the measurement because no Doppler broadening was added in the simulation. Also, Fig. 6.1 shows the transition from below the critical angle to angles larger than the critical angle. This transition behavior is not included in Eq. 6.2, since it is derived from the Fresnel equations which only apply for a homogeneous medium. Thus, the total internal reflection above the critical angle forcing an evanescent field to exponentially decay into the second medium cannot be described with the given equation for the reflectivity. However, one can qualitatively see that for angles below the critical angle β is real. So the quotient χ/β contributes with the real part of the susceptibility, whereas angles above the critical angle lead to an absorptive feature corresponding to $\mathrm{Im}(\chi)$.

6.1. Temperature Dependence

There are two temperatures that are monitored: The reservoir T_{res} and the cell temperature T_{cell}. Both are actively regulated via sensors and temperature controllers with 0.1°C precision. By heating the reservoir with solid/liquid rubidium inside one can control the density. The purpose of separate heaters is to prevent condensation at cold spots. T_{cell} is always 30°C above T_{res}. The accessible cell temperature range in this experiment spans from room temperature to 300°C [43]. The maximum

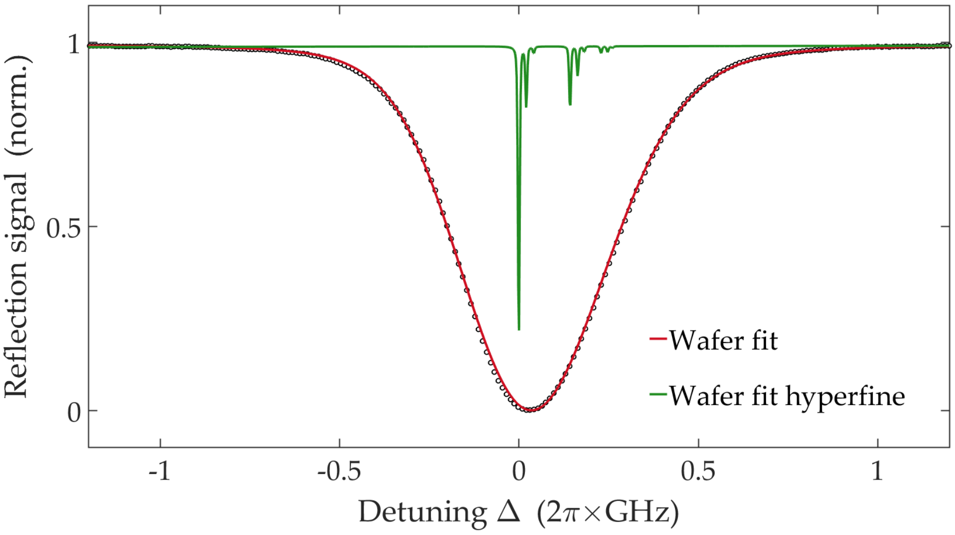

Figure 6.3.: Evanescent wafer spectrum with fit (red) for ^{85}Rb at $T_{\mathrm{res}} = 100°\mathrm{C}$. The green curve shows each individually fitted hyperfine peak. The probe intensity is 31.8 mW/cm^2 and the pump intensity is 57 mW/cm^2.

temperature is set by the oxidation process of zinc selenide with ambient air.
All spectra in the following sections correspond to the case of total internal reflection with absorptive lineshape. In that way the effects of the evanescent field can be studied.
Fig. 6.3 shows the evanescent signal obtained from the wafer cell. The corresponding fit uses the same fit function as derived for the Doppler-free case, however the spacing of the sub features is different. Since the laser beam configuration is perpendicular now, there is no residual Doppler effect that shifts the line. Instead, the sub features are separated by the actual hyperfine splitting of the 5P states (see appendix). In order to visualize the difference between hyperfine spectrum without residual Doppler shift of the sub features and wafer signal, the green curve is plotted in Fig. 6.3. The green function uses the same fit parameters as the red curve but the width and overall amplitude was changed so the hyperfine structure is visible. $5P_{3/2}$ $F' = 4 \rightarrow 4D_{5/2}$ $F'' = 5$ is still the reference transition at zero detuning for ^{85}Rb. The wafer signal is slightly shifted towards higher energies due to the contribution of the sub features within the Doppler broadened signal.

The temperature dependent measurement aims to find the optimal signal strength and to observe broadening and any possible shift of the spectrum. The former was achieved by increasing the reservoir temperature T_{res} from 50°C to 120°C and by that raising the density at the same time. The probe intensity is constantly at

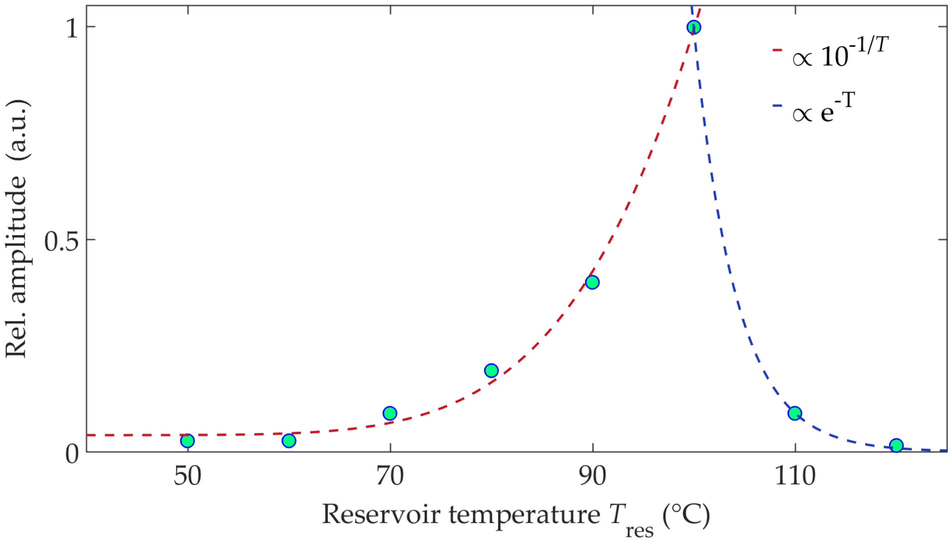

FIGURE 6.4.: Evanescent signal amplitude relative to the maximum amplitude at 100°C. The blue points are statistically averaged points over ten measurements each. The dashed red curve is a fit for reservoir temperatures up to 100°C, and the blue dashed line shows the fit for higher temperatures.

31.8 mW/cm^2 (1 mW) and the pump intensity is $\approx$ 57 mW/cm^2 (45 mW) with a beam waist of 0.5 cm (this is in fact well above the saturation intensity in both cases). However, as one will see the pump power varies substantially along the cell and is actually much smaller in the region of the evanescent field. Operating the probe laser above saturation also increases the signal strength at the cost of (possible) saturation broadening. Due to the huge reflection caused by strongly varying refractive indices, the actual intensity decaying into vapor is much smaller than the input power hitting the prism. Those effects are the topic of the next section.

As one will see in the next section, the achievable temperature range is much smaller than expected. The reason for that is depicted in Fig. 6.4. The data points are statistically averaged signal amplitudes. Each point represents ten statistical measurements. The maximum signal strength is achieved around 100°C. Above that temperature, the amplitude decreases again. This is due to the enhanced absorption of the pump laser at higher densities. The probability of 780 nm photons reaching the evanescent field on the other side of the vapor cell decreases. Therefore, one finds less atoms excited to 5P states within the evanescent field which penetrates roughly 1 μm into the vapor. In order to verify a signal increase purely caused by the density in Fig. 6.4, the temperature dependence of the signal is compared to

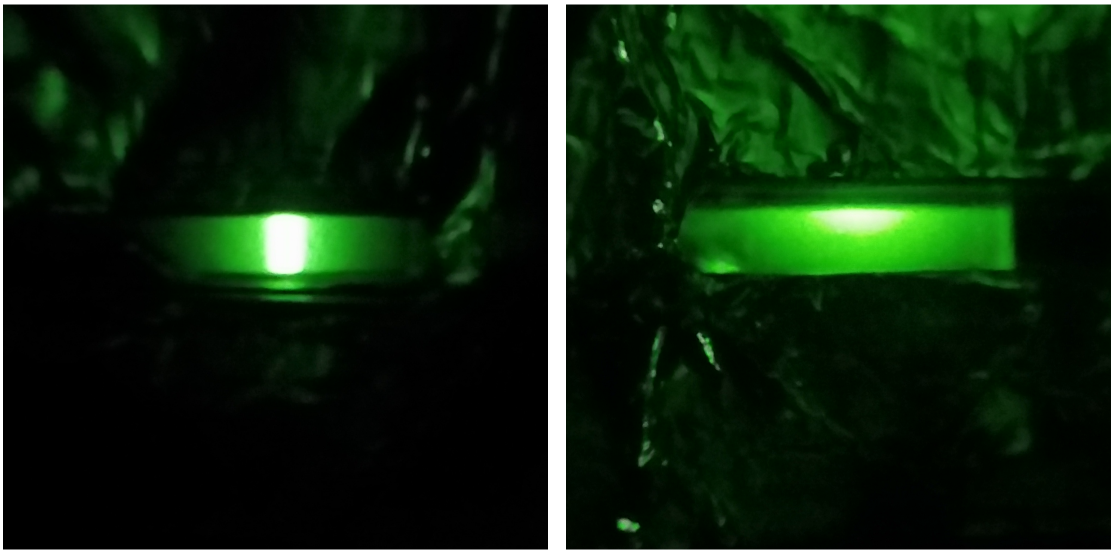

Figure 6.5.: Infrared picture of the pump beam propagating through the cell from above with the same power in both pictures. Left: Low density at $T_{\mathrm{res}} = 50°\mathrm{C}$. Right: High density at $T_{\mathrm{res}} = 130°\mathrm{C}$.

the measured data up to 100°C. The density rises monotonously as

$$n \propto 10^{-\frac{1}{T_{\mathrm{res}}}}. \tag{6.3}$$

This dependency is taken for the vapor pressure p of ^{85}Rb from [39]. For an ideal gas, the pressure p is proportional to the density n. Equally, the signal amplitude scales linearly with the density. To verify this tendency the red curve was fitted to the data up to 100°C with

$$f(T_{\mathrm{res}}) = 10^{-\frac{a}{T_{\mathrm{res}}}+b} + c. \tag{6.4}$$

For temperatures above 100°C, the dense vapor can be described by Beer's law with a fit function $f(T_{\mathrm{res}}) = \exp(-a(T_{\mathrm{res}} - T_0))$. The fit parameters in Eq. 6.4 follow the usage of empirical parameters in [39]. The parameters of the second fit function describe a temperature dependent absorption aT_{res} for a fixed length and the temperature T_0 describes when the decay starts. At higher densities the absorption coefficient changes for the same propagation length. This tendency is drawn as a blue dashed line in Fig. 6.4 as a guide to the eye. The maximum position is highly dependent on the thickness of the cell (here: 5 mm). A thinner cell leads to less absorption for a fixed absorption coefficient, and therefore allows to reach larger amplitudes at higher temperatures before decaying exponentially.

Fig. 6.5 shows infrared pictures of the pump beam propagating from top to bottom through the cell. For low densities (red dashed line in Fig. 6.4) the pump beam is clearly visible in the left picture. The strong absorption of the pump beam at high densities can bee seen in the right picture. Here, the pump beam does not reach the lower part of the cell and is more diffused. That diffused light is the fluorescence of the rubidium atoms excited to the 5P state.

6.1.1. Broadening

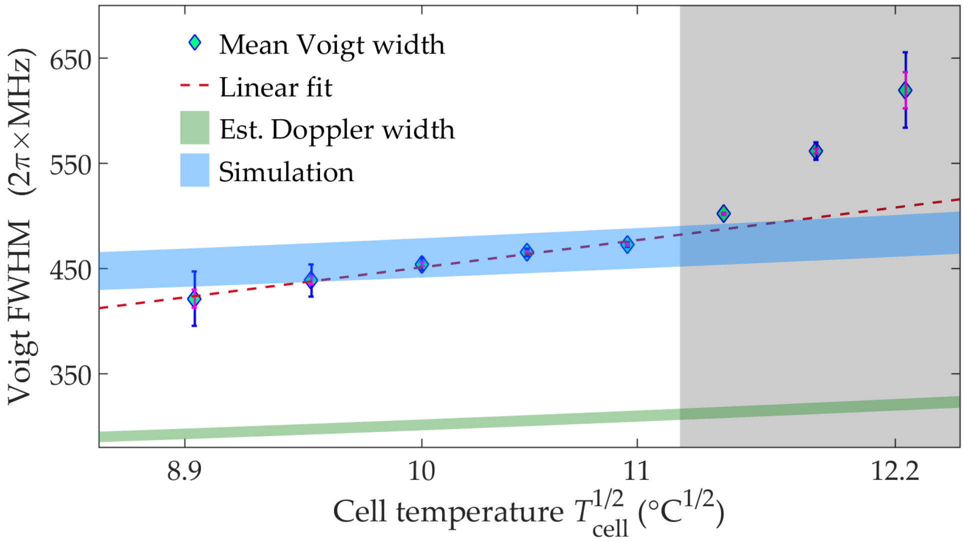

Figure 6.6.: Fitted Voigt width plotted over $\sqrt{T_{\text{cell}}}$. Fit errors are marked with magenta error bars and the standard deviation of ten measurements for each point is labeled with blue error bars. The green area shows the predicted Doppler width alone, whereas the bright blue area adds an expected transit time and power broadening to the Doppler width. The gray shaded area tags the case where density broadening effects dominated the broadening of the spectrum.

This section shares the data with the previous section. This means both laser powers are the same and again, each measured point is a statistical average over ten measurements where no parameters were changed. The reservoir temperature T_{res} was changed in steps of 10°C together with the cell temperature T_{cell}. Due to the fact that both temperatures were gradually increased one can not fully separate Doppler and density broadening. The latter occurs at high densities [44].
The Doppler broadening is expected to be proportional to the square root of the cell temperature T_{cell} as one can see in the 'Atoms in Motion' theory section. For low

densities one can almost neglect contributions from the density to the broadening of the lines. Hence, for reservoir temperatures up to $T_{\mathrm{res}} = 90°\mathrm{C}$ ($T_{\mathrm{cell}} = 120°\mathrm{C}$) a linear fit is used as a guide to the eye in Fig. 6.6. The Doppler broadening for this specific case is given by

$$\Delta\omega_{\mathrm{D}} = k_{\mathrm{x}} v = n_{\mathrm{Si}} \frac{2\pi}{\lambda_{1529}} \sin(\theta_{\mathrm{in}}) \sqrt{\frac{8 \log 2 k_{\mathrm{B}} T_{\mathrm{cell}}}{m_{85}}}, \tag{6.5}$$

with the wavelength of the probe laser λ_{1529}, the angle of incidence θ_{in} and the mass of ^{85}Rb. Among all parameters, the incident angle is determined with the least precision in this measurement. For the calculated curves in Fig. 6.6 it was expected to be between 16.7° and 17.3°. The resulting Doppler broadening is plotted as a green shaded area. Clearly, there is an additional mechanism that contributes to the broadening of the spectrum by ≈ 100 MHz. Since the evanescent field has a penetration depth of $d \approx 1.3\ \mu$m for the approximated angle of incidence, transit time effects contribute to the broadening, as well. The influence of the transit time was added via

$$\omega_{\mathrm{T}} = a_0 \frac{v}{d} = \frac{a_0 \lambda}{2\pi \sqrt{(n_{\mathrm{Si}} \sin(\theta_{\mathrm{Si}}))^2 - 1}} \sqrt{\frac{8 \log 2 k_{\mathrm{B}} T_{\mathrm{cell}}}{m_{85}}}, \tag{6.6}$$

with a prefactor of $a_0 = 0.5$ as found in the following 'Angular Dependence' section. The expression for the penetration depth d can be found in the 'Evanescent field' chapter. Both, the transit time and the Doppler broadening scale with the square root of the temperature. The power broadening obtained from the 'Power Dependence' section adds another 40 MHz for 1 mW probe power with a waist of 1 mm.

Together with the Doppler broadening and an additional offset of 90 MHz, this results in the blue shaded area in Fig. 6.6. The same offset arises in the 'Angular dependence' section for the broadening. This extra offset could be attributed to density broadening mechanisms. Aside from the offset, the curve is in good agreement with the measured data including the statistical error bars and is consistent with the measurements of the width in the following sections. The error bar is larger at the beginning and towards the end due to a much smaller signal to noise ratio. The slope of the fitted curve is lager than the slope of the calculated area. This indicates that other temperature dependent broadening mechanisms could affect the spectrum at lower temperatures. A possible additional broadening effect will be mentioned in the next section.

6.1.2. Frequency Shift

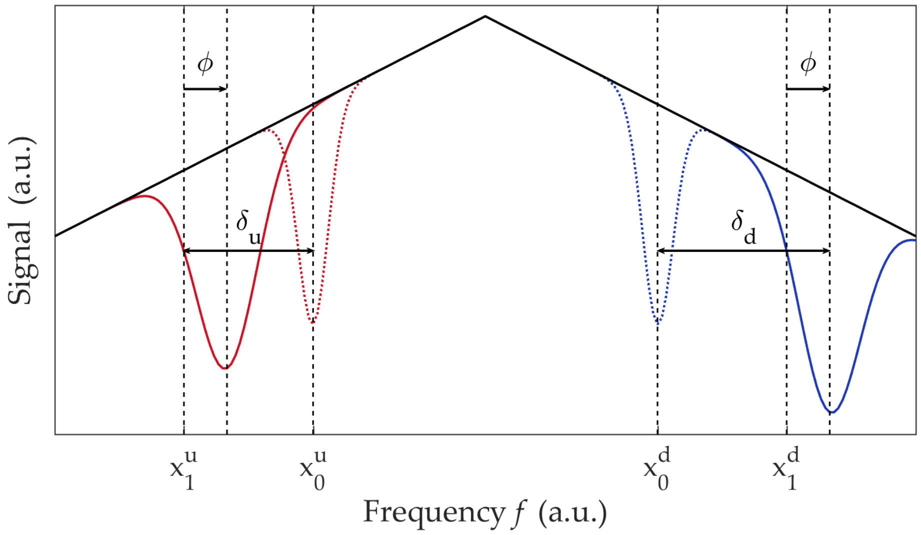

FIGURE 6.7.: Schematic spectrum resembling the measured data to visualize the extraction of the shift. The actual peak positions are marked on the x-axis for ramp up (red) and ramp down (blue). The dashed curve stands for the reference and the solid curve for the wafer signal. A systematic delay ϕ affects only the wafer signal on both ramps.

A detailed derivation will be given on how to extract the shift from the measured data.
Fig. 6.7 shows a schematic screenshot from the oscilloscope. Both, ramp up and down are recorded simultaneously. The reason for that is the fixed delay $\phi \geq 0$ from electronics, especially from the Lock-in amplifier that was used for the wafer signal detection. Here, the broad red curve stands for the wafer signal and the narrow red dashed curve for the reference signal. The same holds for the other ramp in blue. The actual position of the wafer signal is x_1 (u for ramp up and d for ramp down) without any fixed delay. As depicted in Fig. 6.7, that delay causes both ramps to exhibit different shifts. Therefore, it is crucial to analyze both ramps for shift measurements. The position of the reference (main) peak is given by x_0. There are two ways to calculate the real atomic shift: Taking the average of both absolute values of the shift for ramp up and down or extracting the difference in the actual shift (positive and negative). Former yields

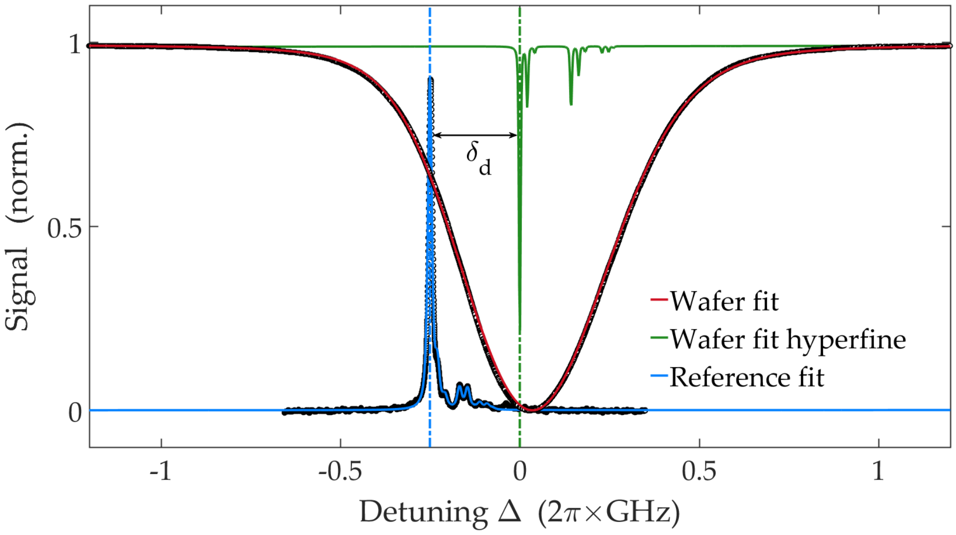

FIGURE 6.8.: Measured shift δ_d between reference and wafer signal with corresponding fits at 100°C for ramp down.

$$\begin{aligned}\delta^{(1)} &= \frac{1}{2}(|\delta_\mathrm{u}| + |\delta_\mathrm{d}|)\\ &= \frac{1}{2}(|x_0^\mathrm{u} - (x_1^\mathrm{u} + \phi)| + |x_0^\mathrm{d} - (x_1^\mathrm{d} + \phi)|)\\ &= \frac{1}{2}(|-x_0^\mathrm{d} + x_1^\mathrm{d} - \phi| + |x_0^\mathrm{d} - x_1^\mathrm{d} - \phi|),\end{aligned} \tag{6.7}$$

with δ_u and δ_d as observed shift (see Fig. 6.7) for ramp up and down, respectively. The detuning axis increases from left to right and is always positive. In the last step $x_0^\mathrm{u} - x_1^\mathrm{u} = -(x_0^\mathrm{d} - x_1^\mathrm{d})$ is used. This calculation of the shift only provides the real shift if the actual shift is larger than the delay $|x_0^\mathrm{u} - x_1^\mathrm{u}| > \phi$.
The second method reads

$$\begin{aligned}\delta^{(2)} &= \frac{1}{2}(\delta_\mathrm{u} - \delta_\mathrm{d})\\ &= \frac{1}{2}(x_0^\mathrm{u} - x_1^\mathrm{u} - \phi - x_0^\mathrm{d} + x_1^\mathrm{d} + \phi)\\ &= \frac{1}{2}(-x_0^\mathrm{d} + x_1^\mathrm{d} - x_0^\mathrm{d} + x_1^\mathrm{d})\\ &= x_1^\mathrm{d} - x_0^\mathrm{d}.\end{aligned} \tag{6.8}$$

The same condition as for the first case is used in the next to last step. The factor 1/2 arises due to the fact that one calculates the difference between a positive (δ_u)

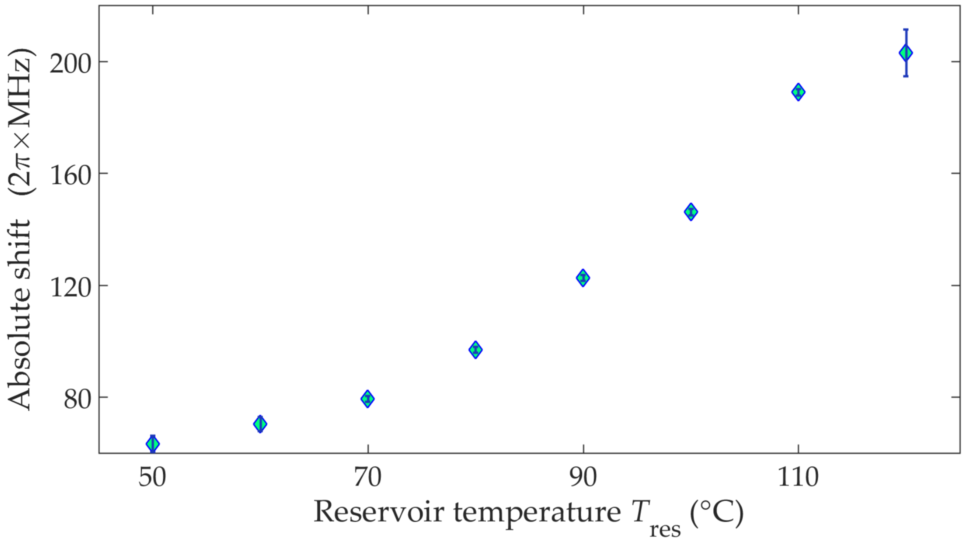

Figure 6.9.: Absolute shift towards higher energies for increasing reservoir temperature. Each point is a statistical average of ten measurements.

and negative value (δ_{d}). Since $\delta^{(2)}$ has no restriction for the ratio between the actual shift and the delay, this is the chosen method to extract the shift.

Fig. 6.8 shows the actual transmission spectrum of the wafer signal and the absorption spectrum of the reference cell with corresponding fits. The shift refers to the spacing between the cyclic hyperfine transition of the reference (blue) and the wafer signal. Here, the shift δ_{d} for ramp down is shown as the difference in the main peak positions of the hyperfine spectrum. Since the residual Doppler sub features occur at an energetically higher level, one can observe a shift towards the blue. For the rising ramp, the spectrum is mirrored so the wafer signal, appearing on the left side of the reference signal, is also shifted to the blue. Exploiting Eq. 6.8 for the calculation of the shift results in Fig. 6.9. Each point stands for the mean value of ten measured shifts, standard deviations are given with error bars. Again, the error bars are larger at the beginning and at the end due to worse SNR at those temperatures. The fit error of ±1 MHz is not plotted here. The vertical axis shows the absolute shift towards higher energies in MHz. The origin of the shift is a redistribution of population in the 5P states. As seen in Fig. 6.5, the pump beam cannot propagate through the dense vapor without being attenuated. The pump laser is locked to the $5S_{1/2}$ F$=3 \rightarrow 5P_{3/2}$ F$' = 4$ transition. Due to the Doppler effect, other dipole allowed 5P hyperfine states are excited as well. Atoms excited to the 5P states spontaneously emit photons which will be reabsorbed further by atoms in the ground state. This process leads to a decrease of the photon number

that only excites the locked transition. So, less 780 nm photons reach the atoms within the evanescent field. Hence, less population can be found in the $5P_{3/2}$ $F' = 4$ state. This effect is smeared out within the Doppler broadened wafer signal. The profile of the shift shows a continuous increase of the shift till 110°C followed by a saturation at higher temperatures. The saturation happens when no photons from the laser, but only fluorescence photons, reach the atoms in the evanescent field on the opposite side of the cell (see right picture in Fig. 6.5). So, the ratio between the populations of the $5P_{3/2}$ $F' = 4, 3, 2$ states changes due to an altered density at the interface. The same observation was made for the commercial cell with perpendicular beam orientation. Thus, the observed blue shift is actually the result of the changing hyperfine population of the 5P states due to the strong absorption of the pump light.
This effect could also lead to a broadening of the spectrum.
Another detailed discussion and measurement of the shift will be given in the 'Angular Dependence' section.

6.2. Power Dependence

6.2.1. 1529 nm Probe

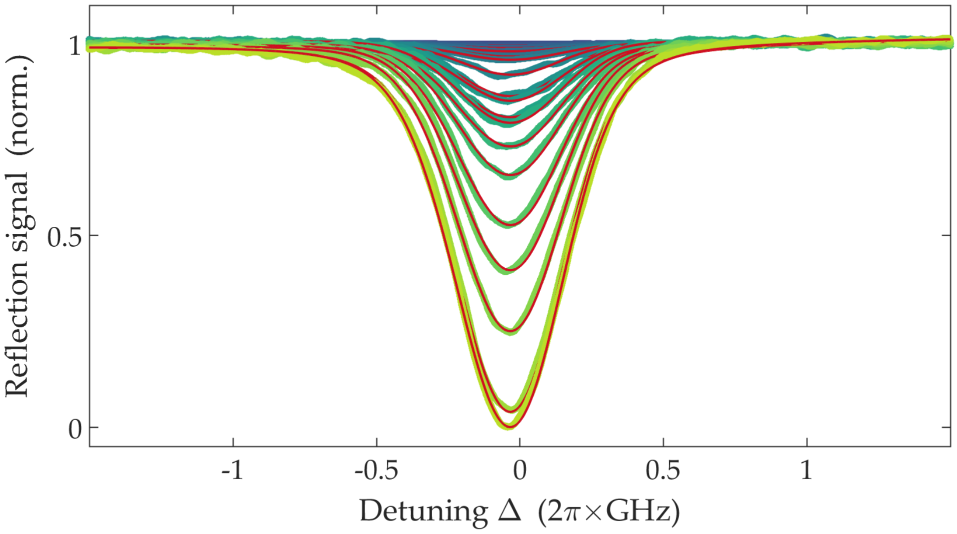

FIGURE 6.10.: Probe power dependent evanescent spectrum with 1 mm beam waist at 100°C. The probe power changes from 1μW (blue) to 5 mW (yellow). The pump intensity is fixed at 57 mW/cm^2. Red curves show the Voigt fits for each measurement.

As observed in the hyperfine reference spectrum, the linewidth depends on the intensity of the probe laser. Fig. 6.10 shows the spectrum for increasing probe power from blue to yellow and corresponding Voigt fits. The probe beam waist is determined to be 1 mm. The power was gradually increased from 1 μW to 5 mW in logarithmic steps.

From the theory section as well as from the hyperfine reference one expects a square root dependence of the width on the intensity. The fit for the Voigt width drawn in Fig. 6.11 works as guide to the eye only. Since the absolute angle of incidence is unknown for that measurement, it is difficult to approximate a reasonable value for the transit time broadening. Nevertheless, the relative change in the width follows the expected square root profile. The vertical dashed line marks the intensity at which the previous measurements for the temperature dependence were made.

In comparison to the saturation curve of the hyperfine signal in the previous chapter, visible broadening starts to appear at higher intensities. The main reason for that is the given values for the power. The horizontal axis shows the intensity measured with the power meter before the cell. So the actual power experienced by atoms in

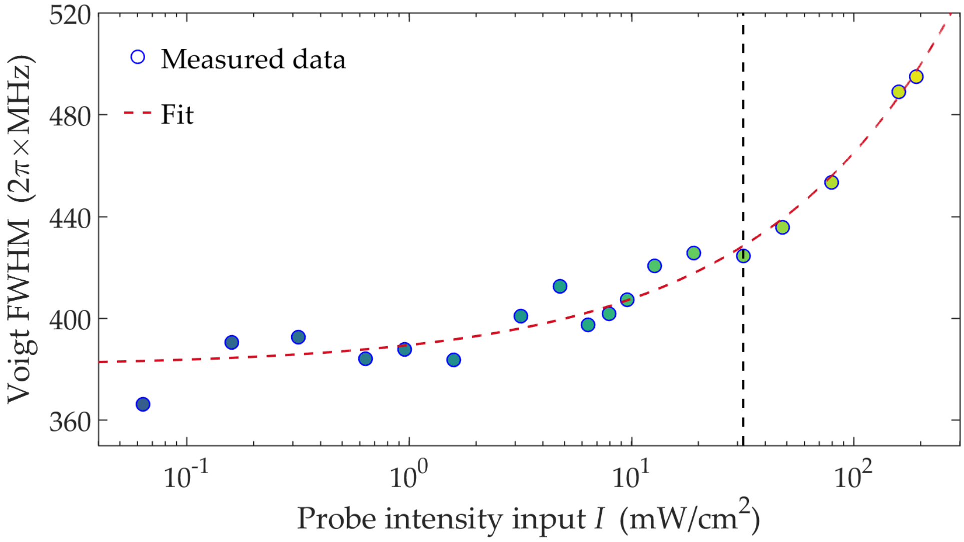

Figure 6.11.: Evanescent signal fitted Voigt width plotted over the probe intensity before the prism. The red dashed line acts as guide to the eye. The vertical black line marks the 1 mW probe power and its corresponding width. The colors match with the curves in Fig. 6.10.

the evanescent field highly deviates from the case of free propagation.

6.2.2. 780 nm Pump

Fig. 6.12 shows the effect of pump power on the evanescent wafer spectrum. The pump power increases in logarithmic steps from 1.5 mW to 45 mW. No signal could be observed below 1.5 mW pump power and 1 mW probe power. Compared to the hyperfine spectrum where an increased pump power leads to splitting of the lines, no splitting could be observed in the Doppler and transit time broadened spectrum for the stated maximum intensity of 57 mW/cm^2. Also, at the beginning one expects a broadening of the line when the splitting is smaller than the width of the peak. In order to observe this effect, an evaluation of the spectrum in Fig. 6.12 was made similar to the probe power dependence in the previous section. However, no power dependent broadening within the given intensity range can be observed. Also, the signal amplitude does not decrease. This was the case for the hyperfine signal for large pump powers. This leads to the conclusion that the used power together with the large beam waist offerers a reasonable power range without Autler-Townes splitting. On the contrary, the intensity seems to be not large enough at higher densities (see Fig. 6.4).
The reason for such a large beam waist is the uncertainty of the position of the

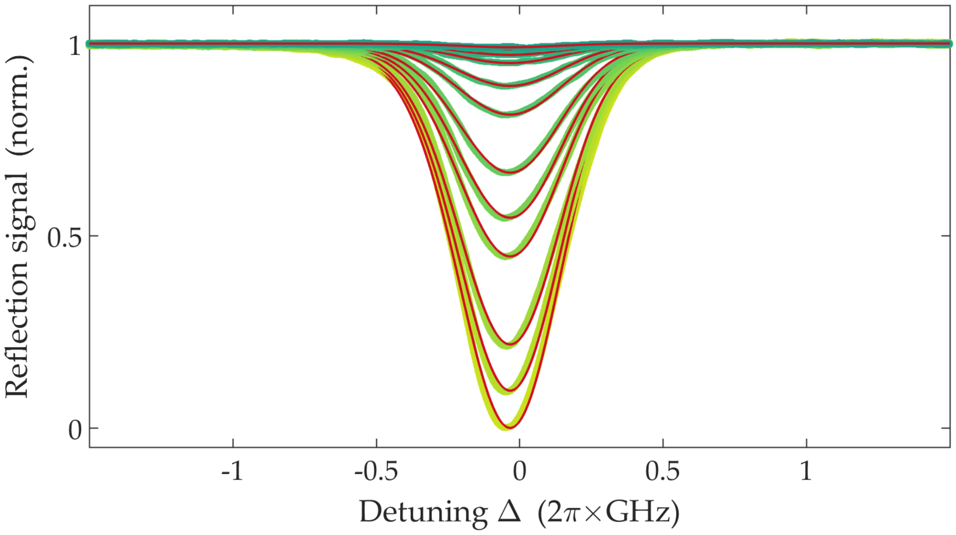

Figure 6.12.: Pump power dependent evanescent spectrum with a beam waist of 0.5 cm at 100°C. The pump power increases from 1.5 mW (green) to 45 mW (yellow). The probe power was kept at 1 mW with a beam waist of 1 mm.

evanescent field. Since the probe beam is coupled under a certain angle of incidence and deflected at every interface with different refractive indices, it is difficult to pin down the evanescent spot. For that reason, a large pump beam was chosen so excitation of atoms to the 5P states in the evanescent field can be guaranteed.

6.2.3. Polarization

The reflectivity derived in the 'Evanescent field' chapter shows a strong dependence on the angle of incidence. The derived reflection coefficients were only given for the extreme cases of fully perpendicular and parallel polarization.

Here, we study the effect of the superposition of both polarizations on the evanescent signal. Any superposition of perpendicular $\hat{e}_s$ and parallel $\hat{e}_p$ polarization can be described with a relative angle between the polarization vectors (see Fig. 6.13). That angle refers to the contribution of parallel and perpendicular linearly polarized light.

The probe beam travels through the following interfaces: Air→ZnSe, ZnSe→ epoxy/glass, Glass→Si and Si→vapor. The reflectivity changes at each interface depending on the relative polarization angle ϕ. In order to give a percentage change in the transmitted power of the evanescent field, one has to calculate the Fresnel equation at every interface.

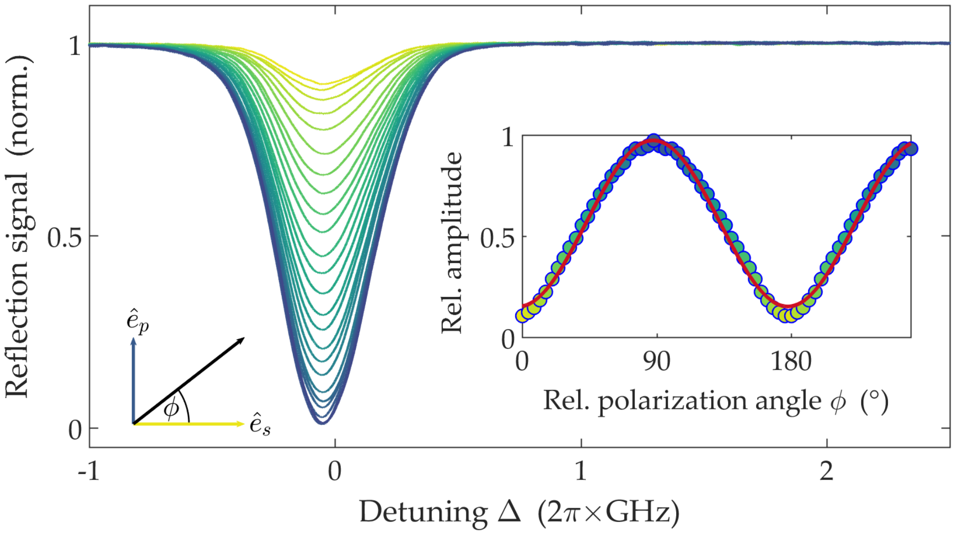

FIGURE 6.13.: Influence of relative the polarization angle between parallel and perpendicular linearly polarized light on the evanescent signal for a fixed angle of incidence. The angle changes from perpendicular (yellow) to parallel (blue) in 4° steps. Inset: Amplitude change relative to the largest peak plotted over the polarization angle ϕ with a sinusoidal fit (red). The color code matches the spectrum.

This section should only give an intuitive comprehension of the change in amplitude, a more detailed discussion can be found in [45].

Fig. 6.13 shows the impact of the relative polarization angle ϕ on the evanescent spectrum for a gradual change from perpendicular (yellow) to parallel (blue) polarization. The angle of incidence is expected to be $\theta_{\text{in}} \approx 62°$ (see Fig. 6.14). The amplitude decreases by roughly 80% from parallel to perpendicular polarization. Continuously altering the polarization between normal and parallel follows a sinusoidal profile, as seen in the inset. The red fit curve only acts as guide to the eye.

In the 'Evanescent field' section the difference in reflectivity is shown for different linear polarizations for all angle of incidence. The angle of incidence is related to the normal on the side of the prism where the probe beam enters. That angle increases from 0° being the normal to 90° towards the apex of the prism (see inset Fig. 6.14). Below 61°, there is total reflection at the Si$\rightarrow$vapor boundary. Perpendicular polarization shows a much smaller reflection than the parallel one. Overall the reflectivity change of $\approx 80\%$ by switching the polarization is expected from the theory, especially close to the critical angle.

6.3. Angular Dependence

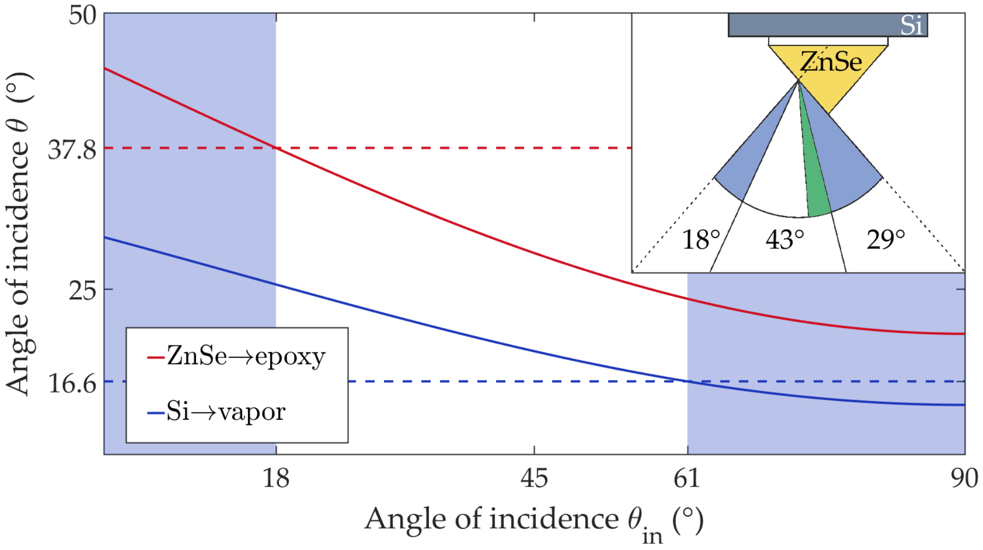

FIGURE 6.14.: Achievable angle of incidence for total reflection at the Si→vapor interface. The red curve shows the angle of incidence at the ZnSe→epoxy interface. The blue curve stands for the angle of incidence at the Si→vapor interface. Dashed lines mark the critical angle for the corresponding interface with matching colors. Inset: Sketch of the prism attached to the cell. The drawn angle of incidence into the prism matches the x-axis and the colors. The green incident angle marks the measurement region.

The angular dependent measurement was done by changing the incident angle into the prism while monitoring the reflected signal from the other side of the prism on the photodiode. The ZnSe prism is used to achieve the desirable angles of incidence into the rubidium vapor of $\theta_{\mathrm{Si}} > 16.6°$. However, due to the epoxy layer that sticks the prism to the Si wafer another interface with possible total reflection is created. Fig. 6.14 shows the angle of incidence into the atomic vapor in blue and the angle of incidence into the epoxy with the red curve. The inset puts the horizontal axis into a geometrical perspective with matching color code. The white window spans all possible angles of incidence for the total reflection at the desired interface. The upper boundary at 61° is set by the critical angle at the Si→vapor transition which is drawn as a blue dashed line. Above that angle, the probe light will be transmitted and the detected reflection shows the dispersive curves at the beginning of this chapter (see Fig. 6.1). The lower bound is set by the critical angle at the ZnSe→epoxy interface marked by the red dashed line. Altogether, this allows for incidence of light within a window of 43°. For comparison, a typical glass prism attached in the same way to the Si wafer would allow a coupling window of 3°. The green angle in the inset of Fig. 6.14 marks the window in which all following angle dependent measurements were performed. This small window is sufficient since the evanescent field changes dramatically close to the critical angle (see 'Evanescent field' chapter).

6.3.1. Absolute Angle of Incidence

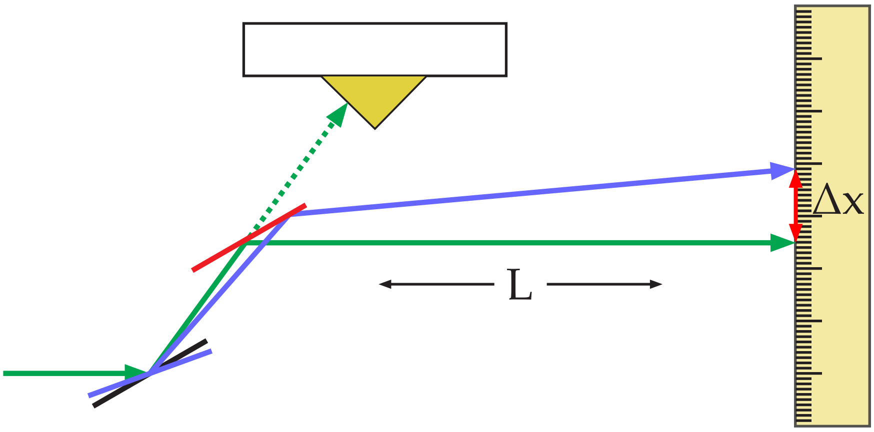

FIGURE 6.15.: Measurement principle for the relative angle of incidence $\theta_{\text{in}}^{\text{rel}}$ into the prism. An additional mirror (red) on a magnetic post is placed in between the coupling mirror (black) and the wafer cell. A tilted coupling mirror (blue) is reflected differently at the red mirror. The change in the beam spot position Δx is measurable on a scale at a distance L.

In oder to obtain a spectrum for a defined angle of incidence, the angle was measured with the method described in Fig. 6.15. An additional mirror (red) is placed before the wafer cell. The position of the reflection is noted on a scale at a distance L. After changing the angle of incidence by changing the coupling mirror into the blue position, the change in beam spot position Δx on the scale is measured. Afterwards, the horizontal position of the coupling mirror is corrected with a translational stage so the beam hits the prism at same position again.
The distance between the coupling and additional mirror is about 5 cm and the scale is usually at a distance of >2 m. Thus, the distance between the mirrors can be neglected and the relative change in the angle of incidence can be calculated from

$$\theta_{\text{in}}^{\text{rel}} = \arcsin\left(\frac{\Delta x}{L}\right). \tag{6.9}$$

This provides relative angles of incidence in steps of 0.5° within the green window in Fig. 6.14. As soon as a dispersive signal appears at the critical angle, the measurement was stopped.

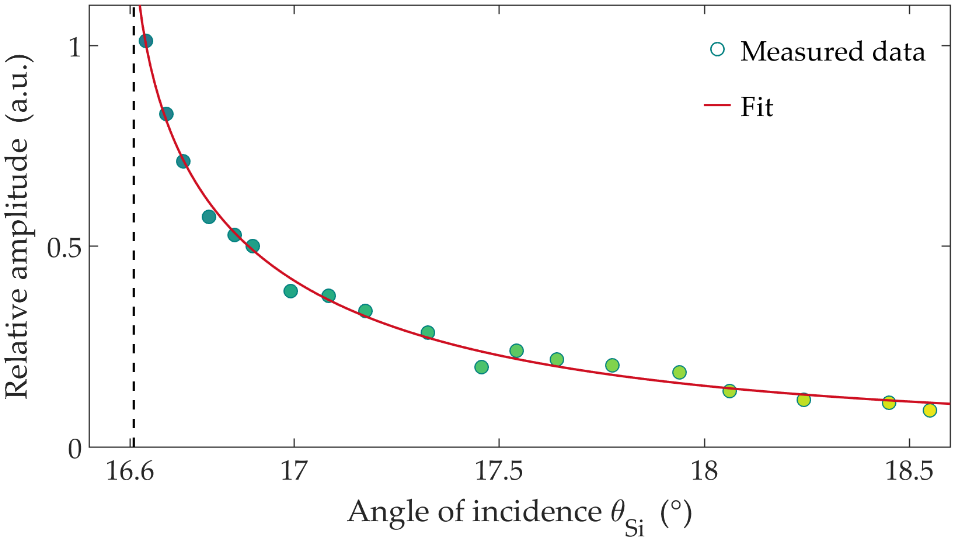

FIGURE 6.16.: Evanescent signal amplitude plotted against the angle of incidence into the rubidium vapor. The red fit function follows the theoretical expression for the intensity. The color code matches the curves in Fig. 6.18. The calculated critical angle is marked as a dashed line.

In order to obtain absolute angles of incidence θ_{Si} into the vapor, the amplitude of the evanescent signal is plotted over the relative angle of incidence.

A fit function

$$\begin{aligned} f(\theta_{\mathrm{in}}^{\mathrm{rel}}) &= I_0 \exp\left(\frac{-1}{d}\right) + \mathrm{Off} \\ &= I_0 \exp\left[\frac{-\lambda}{2\pi n_{\mathrm{Si}}\sqrt{\left(\frac{\sin\theta_{\mathrm{in}}^{\mathrm{rel}}}{\sin\theta_{\mathrm{c}}}\right)^2 - 1}}\right] + \mathrm{Off} \end{aligned} \tag{6.10}$$

is used to calibrate the horizontal axis. The amplitude is fitted with I_0 and the offset with Off. The critical angle at the Si→vapor interface is given by θ_{c}. However, the spectrum changes with the angle of incidence at the Si→vapor interface. Hence, $\theta_{\mathrm{in}}^{\mathrm{rel}}$ is expressed as

$$\begin{aligned} \theta_{\mathrm{in}}^{\mathrm{rel}} = &\arcsin(n_{\mathrm{glass}}/n_{\mathrm{Si}} \sin(\arcsin(n_{\mathrm{ZnSe}}/n_{\mathrm{glass}} \sin(45° - \\ &\arcsin(n_{\mathrm{air}}/n_{\mathrm{ZnSe}} \sin(\theta_{\mathrm{Si}}^{\mathrm{rel}} + \theta_{\mathrm{in}}^{\mathrm{c}} - \theta_{\mathrm{rel}}^{\mathrm{max}} - \Phi)))))). \end{aligned} \tag{6.11}$$

Here, the angle of 45° originates from the right angled ZnSe prism angle. The relative angle of incidence into the vapor $\theta_{\mathrm{Si}}^{\mathrm{rel}}$ is calculated from $\theta_{\mathrm{in}}^{\mathrm{rel}}$ with the same formula but without the following angles: The critical incident angle $\theta_{\mathrm{in}}^{\mathrm{c}} = 61°$

into the prism from Fig. 6.14, the offset given by the maximum relative angle $\theta_{\text{rel}}^{\text{max}} = 11.62°$ and the fitted angle correction Φ. This equation together with Eq. 6.10 is fitted to the relative amplitude of every spectrum. This value for the correction yields $\Phi = 0.154°$ and is subtracted from each relative angle to obtain the absolute angle of incidence. In oder to visualize the precision of the calibrated angles of incidence, the fit function in Eq. 6.10 was fitted to the amplitudes plotted over the calibrated angles of incidence with *only* the amplitude I_0 and offset Off as free fit parameters in Fig. 6.16. The fit shows perfect agreement with the measured amplitudes and therefore, indicates that the presented horizontal axis properly shows the absolute angle of incidence into the rubidium vapor. The expected error in θ_{Si} with the described measurement method is 0.007°.
All following figures and values are calculated with the obtained absolute angles of incidence.

6.3.2. Shift

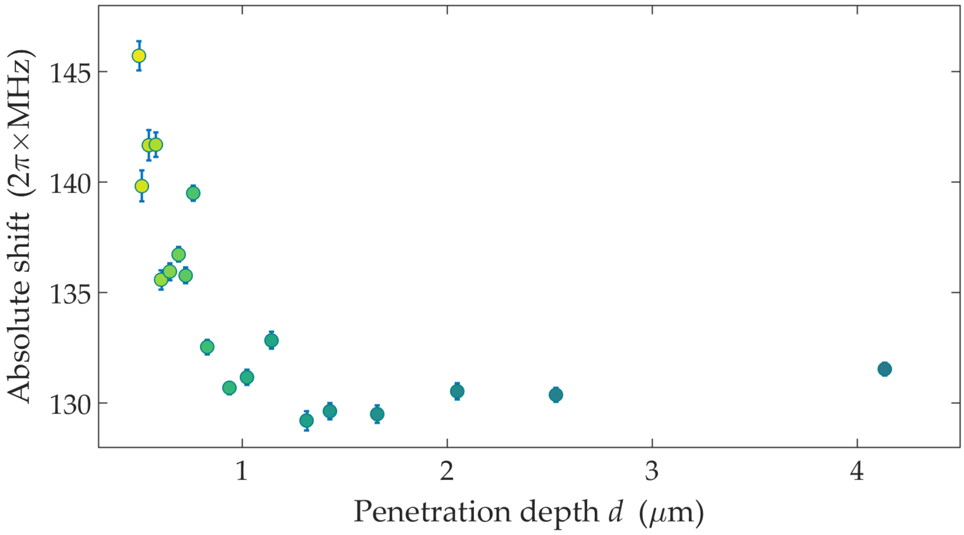

Figure 6.17.: Absolute shift of the wafer signal relative to the reference in dependence of the penetration depth d. The color code matches the spectra in Fig. 6.18.

A possible red shift of the wafer signal could originate from the attractive surface interaction potential due to the Casimir-Polder effect. The goal of this section is to study if any red shift is resolvable.
Fig. 6.17 shows the absolute shift in dependence of the penetration depth d. The

vertical axis reads the absolute shift towards the blue as seen in the shift measurement for different temperatures. The same effect contributes to the observation of a 'blue shift'. The error bar results from fit uncertainties. The colors collaborate with the spectra in Fig. 6.18.

The shift is extracted the same way as described in the 'Shift' section of the temperature dependence. In contrast to the temperature dependent measurement, the data here is not statistically averaged. Nevertheless, a clear decrease in the absolute shift is visible with increasing penetration depth. This means that the shift moves towards a red shift with increasing penetration depth or decreasing angle of incidence. This is the opposite of the theory: An increasing penetration depth corresponds to a smaller surface potential which scales as r^{-3}. Thus, attractive interaction weakens and the red shift should decrease. Since this is not the case in that measurement, this observation most likely originates from the same effect as mentioned in the 'Temperature Dependence' section. The change in the population of the 5P hyperfine states is directly connected to the pump photons reaching the evanescent field. For a larger penetration into the vapor, the chances of atoms interacting with the pump laser photons increases. Hence, the referenced hyperfine transition within the Doppler broadened wafer signal is more dominant and shifts the envelope of the spectrum closer towards the reference cell signal.

In order to overcome this effect one could use a thinner cell, so the pump laser gets less absorbed at higher densities and can still reach the other side of the cell. Also saturation spectroscopy with an additional probe beam coupled in from the other side of the prism would help to overcome the Doppler broadened spectrum and facilitate the referencing of the hyperfine peaks.

6.3.3. Broadening

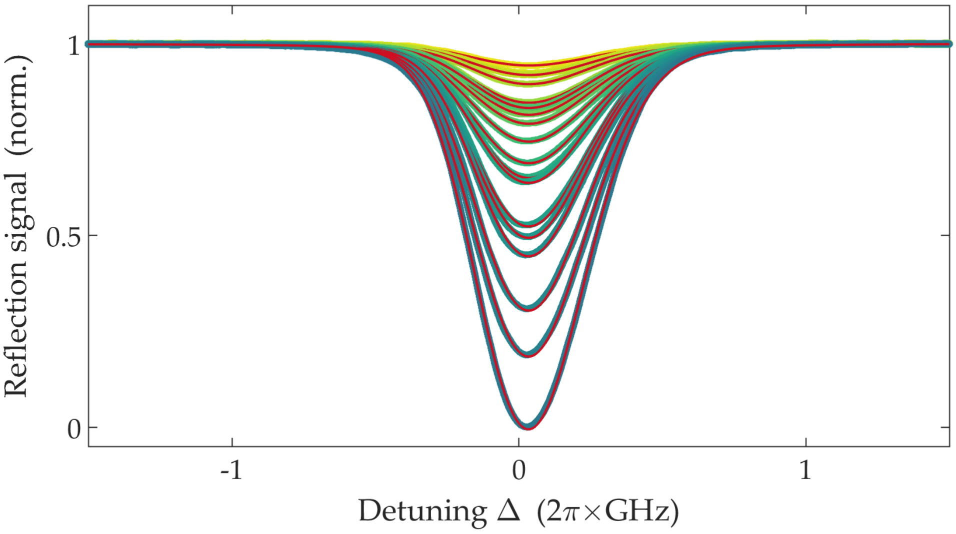

Figure 6.18.: Change in the evanescent signal decreasing angle of incidence θ_{Si} towards θ_{c} from yellow to blue at $T_{\mathrm{res}} = 90°\mathrm{C}$. Red curves show Voigt fits for each spectrum. The probe power is fixed at 1 mW with a beam waist of 1 mm and the pump power is 44 mW with a waist of 5 mm.

The evanescent signal of ^{85}Rb is depicted for different angles of incidence θ_{Si} in Fig. 6.18. The angle of incidence increases from yellow to blue. The 'Evanescent field' chapter shows that the penetration depth d increases when getting closer to the critical angle. The change in the signal amplitude is shown by reference to the angle calibration in the previous section.

A different effect that arises from different angles of incidence is the broadening of the spectrum. This has two reasons: The penetration depth changes which alters the transit time broadening and the wavevector parallel to the surface varies with the angle. This leads to a different contribution of the Doppler broadening. The transit time broadening scales with d^{-1}. Thus, going away from the critical angle towards larger angles leads to less penetration into the atomic vapor and therefore, an increased transit time broadening. Additionally, the wave vector parallel to the surface k_{x} increases further away from the critical angle. The Voigt width is extracted from Fig. 6.18 and plotted over the angle of incidence θ_{Si} in Fig. 6.19.

The simulated curve contains the Doppler broadening for T_{cell} as expressed in the 'Temperature Dependence' section, the transit time broadening

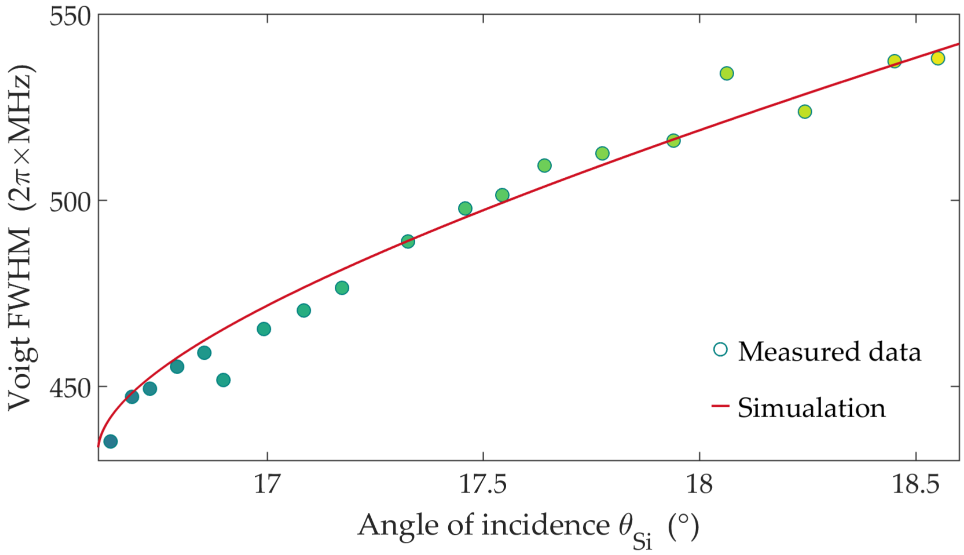

FIGURE 6.19.: Voigt width in dependence on the angle of incidence θ_{Si}. The red curve shows a simulation of the width. The color code matches the spectra in Fig. 6.18.

$$\Gamma_{\mathrm{T}}(\theta_{\mathrm{Si}}) = a_0 \frac{v}{d(\theta_{\mathrm{Si}})}, \tag{6.12}$$

with the same prefactor of $a_0 = 0.5$, and the a power broadening of $\Gamma_I \approx 40$ MHz deduced from Fig. 6.11. However, an additional offset of 90 MHz is added to obtain the matching result in Fig. 6.19. This factor could result from density effects as seen in the temperature dependent plot. The prefactor a_0 is in good agreement with the lineshape in Fig. 6.19. The obtained value for a_0 is used in the previous 'Temperature Dependence' section for the transit time broadening. In general, transit time broadening is only proportional to v/d. The prefactor arises from the fact that atoms, propagating with a certain angle (or direction) through the electric field, experience a different interaction time with the field. It is difficult to calculate the exact prefactor, this is why the prefactor a_0 was fitted here.

7. Conclusion

7.1. Summary

This thesis takes a fundamental step towards spectroscopy of atomic vapors in the vicinity of integrated silicon structures. Previous works in our group have been carried out in the near infrared around 780 nm using Si_3N_4 photonics. However, intrinsic losses due to the absorption of 780 nm light and the fabrication quality of Si_3N_4 set a hard limit to the precision of atomic spectroscopy. To overcome those limitations, in this thesis novel evanescent spectroscopy with pure Si structures and Rb were performed to demonstrate the possibilities of employing the new material and corresponding laser transition from 5P to 4D.
For that purpose a 1529 nm telecom laser was set up. The lasing threshold lies around 92 mA and the maximum power reaches 30 mW which can be increased up to 50 mW. The laser can be scanned within a 10 GHz range.
Together with an existing 780 nm pump laser, saturation two-photon spectroscopy in a 10 cm long reference cell filled with a mixture of ^{85}Rb and ^{87}Rb was performed. The pump laser was locked in all cases while the 1529 nm probe laser was scanned over the 4D states of rubidium. The hyperfine spectrum was fully characterized for both isotopes in co- and counter-propagating configurations of the two lasers. In oder to extract physical properties from the measured spectra, a fit function for the observed 4D spectrum was derived showing a good agreement with the measured data. The spectrum shows probe power broadening above 140 μW/cm^2. An increase in the pump power forces the intermediate 5P states to split. This allows the observation of the Autler-Townes effect in the 4D spectrum.
For evanescent spectroscopy, a new wafer cell was made in-house. A glass window was attached to one side of a glass frame by the method of anodic bonding. A silicon (Si) wafer with 1.5 mm thickness was bonded onto the other side. The cell was evacuated and afterwards filled with rubidium. In order to achieve total internal reflection of the probe beam at the Si→vapor interface, a ZnSe prism was glued to the Si wafer's outer surface. The refractive indices of the used material allow angles of incidence within a 43° window for total internal reflection at the desired interface. The 780 nm pump laser was shone through the glass window

while the 1529 nm probe laser was coupled in through the prism. For angles above the critical angle, the probe laser is totally reflected at the Si→vapor interface with an evanescent field penetrating into the vapor. The atomic signal modifying the reflected probe light is monitored on a photo diode.

Temperature and density dependent measurements were performed for a fixed angle of incidence above the critical angle. Additional broadening of the evanescent wafer signal have been observed due to transit time effects and an enhanced Doppler effect.

The power broadening measurements were done to find the optimum probe intensity regime. Since lots of probe power is lost due to the large change in refractive index propagating through ZnSe, epoxy and Si, the spectrum saturates at larger input intensities compared to the reference cell.

For the last measurement the angle of incidence was changed, first, only slightly around the critical angle of 16.6° at the Si→vapor interface. This allows for the observation of a changing lineshape from dispersive, being below the critical angle, to absorptive above the critical angle. Additional angle dependent measurements above the critical angle were performed in order to study surface effects. The width of the spectrum increases when going further away from the critical angle. This measurement is in good agreement with the theory, which predicts a smaller penetration depth for larger angles and hence, more dominant transit time effects. An expected red shift could not be extracted from the shift measurements due to absorption of pump light within the wafer cell. It leads to an altered population distribution of the hyperfine structure buried within the Doppler broadened wafer signal. This effect makes referencing to the hyperfine signal difficult.

However, this does not limit the possibilities of the measurement in general. To compensate for unwanted effects, thinner cells (here: 5 mm) could be used. Moreover, an additional probe laser coupled in from the opposite side of the prism would provide a hyperfine signal for saturation spectroscopy measurements.

All in all, the desired evanescent two photon spectroscopy at telecom wavelength with the new Si material and rubidium 4D states was demonstrated without any unexpected limitations.

The results of this thesis pave the path to experiments with integrated silicon structures. The last sections briefly explain the follow up studies on integrated silicon structures and silicon nitride (Si_3N_4) cavities.

7.2. Outlook

7.2.1. Silicon Waveguides

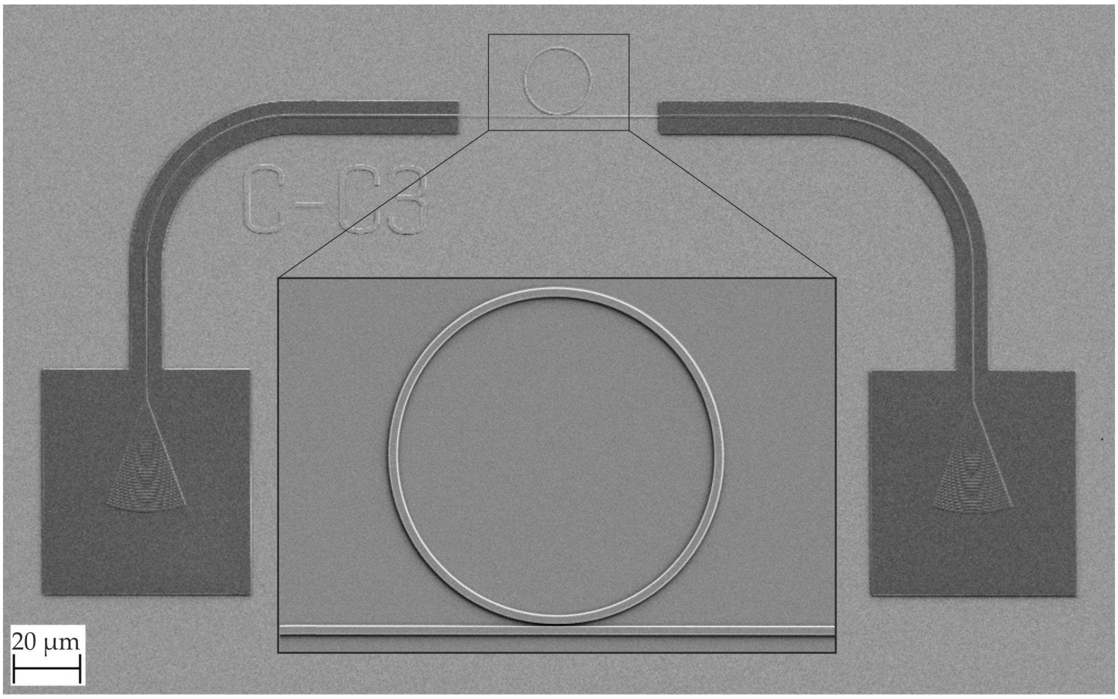

Figure 7.1.: Scanning electron microscope (SEM) picture of a pure Si bus waveguide and the ring resonator. The light is coupled into and out of the structure via the triangular grating couplers.

Fig. 7.1 shows a SEM picture of an already fabricated Si ring resonator. The 1529 nm probe light will be coupled through one of the the grating coupler. The 780 nm pump will illuminate the structure from above, similar to the studied beam configuration in this thesis. The waveguide carries the guiding mode through the whole structure with a tightly bound evanescent field on the surface of the waveguide which interacts with the atoms around the structure.

The dark gray layer consists of SiO_2. The purpose of this layer is to prevent atom light interaction in unwanted regions, especially around the couplers. The inset magnifies the ring resonator that is coupled via the bus waveguide. The evanescent tail of the waveguide mode is coupled through the tiny gap between the ring and the bus waveguide into the resonator.

An additional aluminum layer will be deposited on top of the grating couplers. This layer will prevent the light, scattered at the grating couplers, to interact with the atoms. Also, an additional sapphire layer will be added on top of the whole structure to prevent rubidium atoms attaching to the surface of the structure.

7.2.2. Photonic Crystal Waveguides

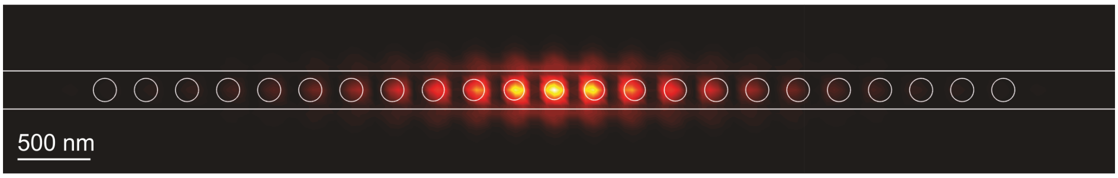

Figure 7.2.: First design of a high Q-factor photonic crystal cavity with simulated electric field intensity.

Typically, atom light interaction happens in the weak coupling regime, as it is the case for the presented ring resonator. However, one aims to access the strong coupling regime with more sophisticated structures described in this section. The simulation of the photonic crystal depicted in Fig. 7.2 is a suitable candidate. The presented structure exhibits a tunable band structure. Its resonance frequency can be adjusted by the size of the holes and their spacing to each other. The electric field is tightly concentrated within the holes and allows potentially strong coupling to atoms traveling through the holes. The laser will be coupled through the side of the structure.

Generally, nanophotonic cavities are capable of inducing strong interactions between single atoms and photons, allowing studies on cavity quantum electrodynamics (QED). The strong concentrated fields can be used to trap atoms close to the surface. This application enables integrated trapped atoms experiments.

A. Rubidium Data

A.1. Physical Properties

All relevant properties of rubidium that were used for calculations in this thesis are listed in the following table.

Isotope	^{85}Rb	^{87}Rb
Relative Natural Abundance	72.17 %	27.83 %
Atomic Mass m	$1.4099931 \cdot 10^{-25}$ kg	$1.443160 \cdot 10^{-25}$ kg
Nuclear Spin I	5/2	3/2

$5S_{1/2} \rightarrow 5P_{3/2}$ Transition	
Lifetime τ_{SP}	26.2348 ns
Transition Dipole Moment d	$3.58425 \cdot 10^{-29}$Cm
Saturation Intensity (π-polarized) I_{sat}	2.50399 mW/cm^2

$5P_{3/2} \rightarrow 4D_{5/2}$ Transition	
Lifetime τ_{PD}	84.0 ns
Transition Dipole Moment d	$4.75459 \cdot 10^{-29}$Cm
Saturation Intensity (π-polarized) I_{sat}	0.138 mW/cm^2

TABLE A.1.: Atomic and optical properties of rubidium for both studied isotopes.

The numbers for the D$_2$-line ($5S_{1/2} \rightarrow 5P_{3/2}$ transition) are taken from Steck [39,46] whereas the lifetime of the 4D states was found in [47]. The reduced transition dipole matrix element is given by $\mathbf{d} = \langle J || e\mathbf{r} || J' \rangle$, with the displacement vector $\mathbf{r}$. However, a factor of 1/3 arises for the case of linearly polarized light (π-polarized) where only one component of the dipole moment $\mathbf{d}$ interacts with the light field. The elemental charge is given by e. The saturation intensity for π-polarized light can then be calculated via

$$I_{\text{sat}} = \frac{c\epsilon_0\hbar^2}{4\tau^2|\hat{e}\mathbf{d}|^2} \tag{A.1}$$

for a two level system. A derivation of this expression for the saturation intensity will be given in the 'Atom Light Interaction' chapter. The speed of light is given by c, the vacuum permittivity is given by ϵ_0, the lifetime of the excited state is given by τ, the polarization vector is given by $\hat{e}$, and $\hbar$ stands for the reduced Planck constant. The saturation intensity for the 4D state was calculated assuming a two level system with $5P_{3/2}$ being the homogeneously populated ground state. The 5P to 4D transition saturates at much lower intensities due to the much larger life times $\Gamma \propto \omega_0^3 |\langle J| |e\mathbf{r}| |J'\rangle|^2$ of the 4D states ($\approx$ 3 times larger than for the D_2 line) and a correspondingly larger dipole moment. The resonant wavelength is given by ω_0.

A.2. Hyperfine Level Spacing

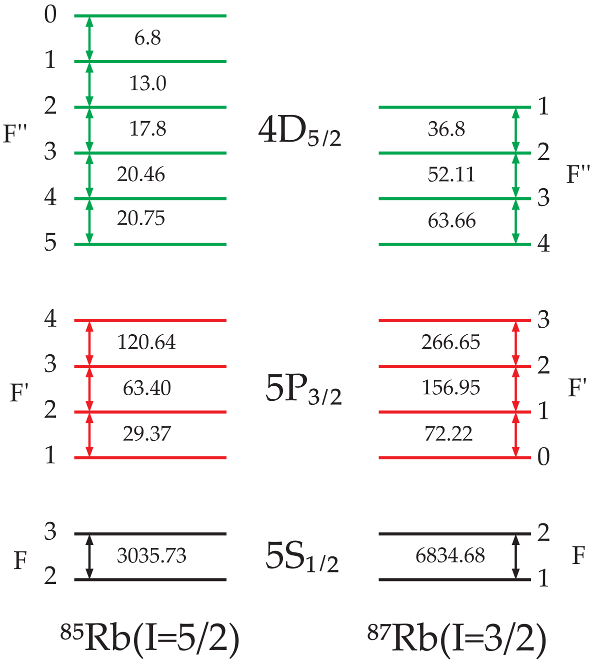

Figure A.1.: Relative hyperfine frequency spacing f in MHz for the ground state $5S_{1/2}$ and the two excited states $5P_{3/2}$ and $4D_{5/2}$ of ^{85}Rb and ^{87}Rb.

Fig. A.1 shows all relative hyperfine levels for the possible $5S_{1/2}$, $5P_{3/2}$, and $4D_{5/2}$ states. All calculations and fits in this work use those frequency values. The numbers for the ground state $5S_{1/2}$ and first excited state $5P_{3/2}$ are taken from [39] and [46] for both isotopes. The spacings for the second excited state, $4D_{5/2}$, in particular the hyperfine spacings between F" = 3,4,5 (^{85}Rb) and F"= 2,3,4 (^{87}Rb) were taken from [48], and the levels F"= 0,1,2,3 (^{85}Rb), and F"= 1,2 (^{87}Rb) are from [40].

Bibliography

[1] Andrew D. Ludlow *et al.* Optical atomic clocks. *Rev. Mod. Phys.*, 87, 2015.

[2] James Camparo. The rubidium atomic clock and basic research. *Physics Today*, 60, 2007.

[3] T.M. Fortier *et al.* Precision Atomic Spectroscopy for Improved Limits on Variation of the Fine Structure Constant and Local Position Invariance. *Phys. Rev. Lett.*, 98, 2007.

[4] L. Cacciapuoti and C. Salomon. Atomic clock ensemble in space. *J. Phys. Conf. Ser.*, 327, 2011.

[5] D. Barredo *et al.* Electrical Readout for Coherent Phenomena Involving Rydberg Atoms in Thermal Vapor Cells. *Phys. Rev. Lett.*, 110, 2013.

[6] J.A. Seclacek *et al.* Microwave electrometry with Rydberg atoms in a vapour cell using bright atomic resonances. *Nat. Phys.*, 8, 2012.

[7] A. Horsley *et al.* Imaging of relaxation times and microwave

field strength in a microfabricated vapor cell. *Phys. Rev. A*, 88, 2013.

[8] Johannes Schmidt *et al.* Proof of concept for an optogalvanic gas sensor for NO based on Rydberg excitations. *Submitted*, 2018.

[9] Fabian Ripka *et al.* A room temperature single-photon source based on strongly interacting Rydberg atoms. *Submitted*, 2018.

[10] Ralf Ritter *et al.* Atomic vapor spectroscopy in integrated photonic structures. *Appl. Phys. Lett.*, 107, 2015.

[11] Ralf Ritter *et al.* Coupling thermal atomic vapor to an integrated ring resonator. *New. J. Phys.*, 18, 2016.

[12] Ralf Ritter *et al.* Coupling thermal atomic vapor to slot waveguides. *Phys. Rev. X*, 8, 2018.

[13] H. H. Li. Refractive index of silicon and germanium and its wavelength and temperature derivatives. *J. Phys. Chem. Ref. Data*, 9, 1980.

[14] Philip E. Ciddor. Refractive index of air: new equations for the visible and near infrared. *Appl. Optics*, 35, 1996.

[15] D. T. F. Marple. Refractive Index of ZnSe, ZnTe, and CdTe. *J. Appl. Phys.*, 35, 1964.

[16] Wolfgang Demtröder. *Experimentalphysik 2*. Springer, 2009.

[17] G. S. Agarwal. Rotating-Wave Approximation and Spontaneous Emission. *Phys. Rev. A*, 4, 1971.

[18] Wolfgang Nolting. *Theoretical Physics 8*. Springer, 2007.

[19] G. Lindblad. On the generators of quantum dynamical semigroups. *Commun. Math. Phys.*, 48, 1976.

[20] M. Fleischhauer, A. Imamoglu, and J. P. Marangos. Electromagnetically Induced Transperency: Optics in Coherent Media. *Rev.Mod. Phys. 77, 633*, 2005.

[21] Schott Technical Glass Solutions GmbH. Schott Borofloat 33. Schott, Jena, Germany, 2017.

[22] Renate Daschner. Addressable Rubidium vapor cells for optical and electrical read-out of Rydberg excitations. *Universität Stuttgart*, 2015.

[23] Epoxy Technology Inc. EPO-TEK 301-2. Billerica, MA, USA, 2017.

[24] J. E. Rogers R.M. Sternheimer and T. P. Das. Effect of the atomic core on the fine-structure splitting for excited nd and nf states of the alkali-metal atoms. *Phys. Rev. A*, 17, 1977.

[25] R. Gupta K.H. Loao, L.K. Lam and W. Happer. Cascade Anticrossing Measurement of the Anomalous Hyperfine Structure of the 4^2D State of Rubidium. *Phys. Rev. Lett.*, 32, 1974.

[26] H.Lundberg K. Fredriksson and S. Svanberg. Fine- and hyperfine-structure investigation in the 5^2D-n^2F series of cesium. *Phys. Rev. A*, 21, 1979.

[27] Taelsul Lee *et al.* Theory of negative fine and hyperfine structure in excited states of rubidium: 4^2D state. *Phys. Rev. A*, 14, 1975.

[28] Wolfgang Demtröder. *Laserspektroskopie 2.* Springer, 2013.

[29] Heung-Ryoul Noh and Han Seb Moon. Calculation of line shapes in double-resonance optical pumping. *Phys. Rev. A*, 80, 2009.

[30] Paul Siddons *et al*. Absolute absorption on rubidium D lines: comparison between theory and experiment. *J. Phys. B-At. Mol. Opt.*, 41, 2008.

[31] J.J. Sakurai. *Modern Quantum Mechanics.* Addison-Wesley, 1994.

[32] D.M. Brink and G.R. Satchler. *Angular Momentum.* Oxford, 1994.

[33] J.J. de Swart. The Octet Model and its Clebsch-Gordan Coefficients. *Rev.Mod.Phys.*, 35, 1963.

[34] C.E.J. Mitchell A.B. McLean and D.M. Swanston. Implementation of an efficient analytical approximation to the Voigt function for photoemission lineshape analysis. *J. Electron Spectrosc.*, 69, 1994.

[35] M. Rosete-Aguilar R. Diaz-Uribe and R. Ortega-Martinez. Position sensing of a Gaussian beam with a power meter and knife edge. *Rev. Mex. Fis.*, 39, 1992.

[36] J.J. Oliviero and R.L. Longbothum. Empirical fits to the Voigt line width: A brief review. *J. Quant. Spectrosc. Ra.*, 17, 1977.

[37] S. H. Autler and C. H. Townes. Stark Effect in Rapidly Varying Fields. *Phys. Rev.*, 100, 1955.

[38] E.T. Jaynes and F.W.Cummings. Comparison of quantum and semiclassical radiation theories with application to the beam maser. *P. IEEE.*, 51, 1963.

[39] D.A.Steck. Rubidium 85 D Line Data, 2013. available online at http://steck.us/alkalidata, Version 2.1.6.

[40] Jie Wang *et al*. Determination of the hyperfine structure constants of the ^{87}Rb and ^{85}Rb 4D$_{5/2}$ state and the isotope hyperfine anomaly. *Phys. Rev. A*, 90, 2014.

[41] Heung-Ryoul Noh and Han Seb Moon. Discrimination of one-photon and two-photon coherence parts in electromagnetically induced transparency for a ladder-type three-level atomic system. *Opt. Express*, 19, 2011.

[42] Ryan James Thomas. Observation and characterization of electromagnetically induced transparency using evanescent fields. *University of Calgary*, 2012.

[43] P.P. Gorbik *et al*. Electron-Emission and Cathodoluminescent Properties of ZnO Films Prepared by Oxidation of ZnSe and ZnS. *Inorg. Mater+*, 37, 2001.

[44] M.Gorris-Neveux *et al*. Doppler-free reflection spectroscopy of rubidium D1 line in optically dense vapour. *Opt. Commun.*, 134, 1997.

[45] F. Schuller G. Nienhuis and M-Ducloy. Nonlinear selective reflection from an atomic vapor at arbitrary incidence angle. *Phys. Rev. A*, 38, 1988.

[46] D.A.Steck. Rubidium 87 D Line Data, 2015. available online at http://steck.us/alkalidata, Version 2.1.5.

[47] O.S. Heavens. Radiative Transition Probabilities of the Lower Excited States of the Alkali Metals. *J. Opt. Soc. Am.*, 51, 1961.

[48] Won-Kyu Lee and Han Seb Moon. Measurement of absolute frequencies and hyperfine structure constants of $4D_{5/2}$ and $4D_{3/2}$ levels of ^{87}rb and ^{85}rb using an optical frequency comb. *Phys. Rev. A*, 92, 2015.

Danksagung

An erster Stelle möchte ich mich bei Tilman Pfau bedanken, sowohl für die Möglichkeit eine Masterarbeit an dem Institut zu absolvieren, als auch für die vielen hilfreichen Diskussionen in unseren Meetings.

Mein besonderer Dank gilt Robert, der das Thema meiner Masterarbeit vorantreibte und mir jegliche Freiheit und Mittel zur Verfügung stellte das Projekt in Realität umzusetzen.

Einen herzlichen Dank an Ralf und Hadiseh, die mich bei Problemen unterstützt und beraten haben. Ich danke beiden ebenso für das Korrekturlesen dieser Arbeit.

Genauso möchte ich mich bei Harald bedanken, der jederzeit ein offenes Ohr für mich hatte und mich bei Themen aller Art beraten hat.

Einen besonderen Dank verdienen meine (Nachbar-) Büro-Kollegen Johannes, Markus und Nico. Danke, dass ihr jederzeit offen für Fragen wart und mich auch neben der Masterarbeit unterhalten habt (sowohl positiv als auch negativ).

Ich bedanke mich sehr bei Markus, Hoy-My und Marcel für ihren Beitrag an der Korrektur dieser Arbeit.

Da es so viele andere Leute gibt, denen ich für jegliche Gespräche und Aktivitäten danken möchte, gilt mein Dank allen Mitarbeitern des Instituts, besonders den jetzigen sowie ehemaligen im dritten Stock.

Zu guter Letzt möchte ich mich bei meiner Familie bedanken, die mein Studium möglich gemacht haben und mich jederzeit unterstützt haben.